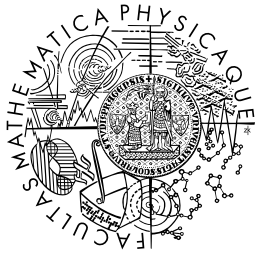

FACULTY
OF MATHEMATICS
AND PHYSICS
Charles University

DOCTORAL THESIS

Lukáš Chlad

Study of transverse flow of kaons in Au + Au collisions at $1.23A\,\mathrm{GeV}$

Nuclear Physics Institute CAS, p.r.i.

Supervisor of the doctoral thesis:	RNDr. Andrej Kugler, CSc.
Study programme:	Particle and Nuclear Physics
Study branch:	Physics

Prague 2021

Title: Study of transverse flow of kaons in Au + Au collisions at 1.23A GeV

Author: Lukáš Chlad

Institute: Nuclear Physics Institute CAS, p.r.i.

Supervisor: RNDr. Andrej Kugler, CSc., Nuclear Physics Institute CAS, p.r.i.

Abstract: The production and propagation of strange hadrons at the threshold energy are important probes of the in-medium hadron's properties and stiffness of the equation of state of nuclear matter. In this thesis, the transverse kaon flow at Au + Au collisions with kinetic beam energy 1.23A GeV measured with the HADES spectrometer is discussed. The motivation for such an analysis and the theoretical introduction are described first, followed by the characterization of the the individual parts of HADES spectrometer. The procedure to identify detected particles from the measured signals is introduced. Finally, the flow analysis and its results are presented. The differential directed and elliptic flow of kaons in measured gold on gold collisions is compared with published data and with kinetic transport model predictions.

Keywords: relativistic heavy-ion collisions, transverse flow, kaon flow

Contents

Introduction

The goal of this thesis is to present the results of an analysis focused on kaon flow measured in Au + Au collisions with kinetic beam energy $1.23A$ GeV by HADES spectrometer.

To achieve this goal, I shall introduce to the reader the problematic of heavy-ion collisions and what is our motivation for such kind of experiments. This introduction will be given in chapter 1 together with a presentation of the basics of Quantum Chromo Dynamics. If one wants to learn something from the experiments, the appropriate description of the phenomena by theory is necessary. In the case of heavy-ion collisions, we might need Statistical Hadronization Models, Kinetic Transport Models, or Relativistic Hydrodynamic Models. A short introduction to all of them will also be part of the first chapter. An overview of current experimental knowledge of kaon flow in heavy-ion collisions at similar energy will be presented as well.

In the following chapter 2, I will briefly describe all subsystems of the HADES spectrometer. Understanding the tools that we are using for the measurement is essential when problems occur and we need to overcome them in the future. That is also why the HADES spectrometer is constantly upgraded, and many members of the HADES collaboration are not only purely focused on the physics analysis of recorder data but also come into contact with the actual hardware. In the last section of the second chapter, I will illustrate the problematic of TOF detector calibration.

Chapter 3 is dedicated to the so-called low-level data analysis and the principles of particle identification from data. Full details are not given, but fundamentals on how to reconstruct particle properties such as mass, charge, momentum, and velocity from registered hits in HADES detectors are described.

The explanation of my analysis starts in chapter 4, where the details of the identification of both charged kaons and short-lived neutral kaons are presented. In the case of charged kaons, the candidates are selected on the basis of the track quality parameters and specific energy loss within the volume of the MDC and TOF detectors. The number of background entries is estimated by fitting the mass spectra. The short-lived neutral kaon candidates are reconstructed using their decay into two charged pions. To suppress the combinatorial background, the neural network was trained on the simulations, and the optimized cuts of the decay topology variables were later applied to the experimental data. The background of pion pair invariant mass spectrum is described with the mixed-event technique.

The next chapter 5 is devoted to the flow analysis. A historical introduction into the field of transverse flow in heavy-ion collisions is presented with the intention to explain the method of flow applied flow analysis in this thesis. I think it is important to explain the theoretical development of the flow analysis, which accompanied the experimental effort in which the increase of collision energy brought several difficulties.

Finally, the chapter 6 starts with the evaluation of systematic uncertainty. This is followed by the presentation of the results on differential kaon flow that are later compared with model predictions.

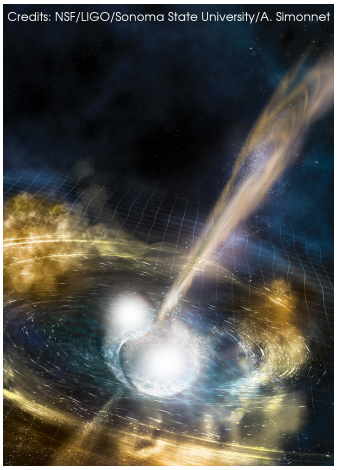

Chapter 1

Hot and dense baryonic matter

1.1 Heavy-ion collisions

To understand the processes that occurred just a few microseconds after the Big bang [1], or that may occur during the recently observed neutron star merge with gravitational waves [2], experiments in laboratories are necessary. The only way to replicate similar conditions is to collide heavy ions (HIC). With the aim of probing the phase-space diagram of nuclear matter and studying the nuclear equation of state, it is needed to study the whole spectrum of HIC using different ions and scan as many interaction energies as possible.

We can identify three stages of HIC: first-chance nucleon-nucleon (NN) collisions, high density (fireball formation and its adiabatic expansion), and freeze-out stage (chemical and kinetic freeze-out). Using the SIS18 accelerator, it is possible to achieve up to three times the density of the nuclear ground state ($\rho \approx 3\rho_0$ where $\rho_0 \approx 0.16\,\mathrm{N/fm^3}$) and temperatures up to $100\,\mathrm{MeV}$[1] [3]. The matter at such extreme conditions creates the so-called fireball which has a very short lifetime $\sim 10^{-22}\,\mathrm{s}$ after which the matter is expanding and cools down. The next important moment happens when the energy of a possible collision is low enough that no inelastic processes are possible and except the decay of resonances, the created particles will not change their nature, this moment is called chemical freeze-out. However, the particles still undergo elastic interactions until the kinetic freeze-out, which is the last milestone of the HIC after which the particles travel unchanged to the detector again except for a possible decay.

An essential measure of HIC is the impact parameter b, which is defined as the distance between the centers of colliding nuclei. With decreasing values of impact parameters, we are speaking about increasing centrality of the collision. When the two nuclei overlap almost completely, we are speaking about a central collision, and when this overlap is only partial, we are speaking about the peripheral collision. Unfortunately, it is not possible with current technology to influence the centrality or to measure directly the impact parameter, hence it must be estimated based on the number of emitted particles (multiplicity). Often used theoretical description which is then compared with experimentally measured

[1] We are using energy units due to the conversion $E = kT$, the room temperature $300\,\mathrm{K} = 25.852\,\mathrm{meV}$.

multiplicity is the Glauber model using Monte Carlo simulations [4]. We also distinguish between the nucleons which go through the reaction zone, which are called participants, and those who only pass around the so-called spectators.

1.1.1 Particle production

The important variable for particle production is the square root of the Mandelstam variable $s = (P_1 + P_2)^2$ [5], where P_1 and P_2 are four vectors of colliding particles. In the case of a fixed target experiment, the center-of-mass energy of the collision can be calculated

$$\sqrt{s} = \sqrt{2E_{\mathrm{kin,beam}} m_{\mathrm{target}} c^2 + (m_{\mathrm{beam}} + m_{\mathrm{target}})^2 c^4}, \tag{1.1}$$

where $E_{\mathrm{kin,beam}}$ and m_{beam} are the kinetic energy and the mass of beam particles and m_{target} is the mass of target particles. In the case of HIC with the same nuclei used as projectile and target, we can define $\sqrt{s_{\mathrm{NN}}} = \sqrt{s}/A$ the center-of-mass energy of NN collisions for easier comparison with elementary interactions (in case of Au+Au collisions with kinetic energy $1.23A$ GeV we obtain $\sqrt{s_{\mathrm{NN}}}\big|_{\mathrm{Au+Au}} = 2.42\,\mathrm{GeV}$). The production of N_{particle} particles is conditioned with the so-called threshold energy

$$\sqrt{s_{\mathrm{thr}}} = \sum_{i=1}^{N_{\mathrm{particle}}} m_i c^2 \tag{1.2}$$

where m_i is the rest mass of each outgoing particle.

Using the equation (1.2), we can calculate the minimal energy of the elementary NN collision needed to produce strange particles, which is of interest in this thesis. Since the NN collision is subject to the strong interaction that preserves the additive quantum number strangeness,[2] the production of only one strange hadron is not possible (except for hidden strangeness, e.g. ϕ-meson which contains $|s\bar{s}\rangle$ pair). Using the nominal values of the masses of strange hadrons [6] and the sum rules of the strong interaction (strangeness conservation $N(s) - N(\bar{s}) = 0$ and baryon number conservation $N(B)_{\mathrm{in}} = N(B)_{\mathrm{out}}$) one can get the threshold energy values for production channels, see table 1.1. From this table we observe that all production channels from free NN collisions are above the available center-of-mass energy in studied Au + Au collisions, therefore, one would expect that the production of strangeness hadrons in this case is not possible. However, in the case of HIC, there are several mechanisms that can provide the additional energy or lower the threshold energy, thus the so-called subthreshold production is observed:

Fermi momentum Nucleons inside nuclei are influenced by the Pauli exclusion principle for fermions, and therefore nucleons are forced to populate higher energy states and gain additional momenta up to $p_{\mathrm{F}} \approx 250\,\mathrm{MeV}/c$.

Multistep processes During the dense stage of HIC, nucleons can be elastically scattered multiple times and gain enough momentum to produce strange hadrons. Within this option, we also include the possibility that an inelastic NN collision produces intermediate resonances like Δ or N^* which then again interact [7].

[2] Hadrons containing anti-quark $\bar{s}$ have $S = +1$ and hadrons with quark s have $S = -1$.

Production channel	$\sqrt{s_{\mathrm{thr}}}$[GeV]	$\sqrt{s_{\mathrm{NN}}}\big\vert_{\mathrm{Au+Au}} - \sqrt{s}_{\mathrm{thr}}$[GeV]
$\mathrm{NN} \rightarrow \mathrm{N\Lambda K^+}$	2.55	-0.13
$\mathrm{NN} \rightarrow \mathrm{N\Lambda K^0}$	2.56	-0.14
$\mathrm{NN} \rightarrow \mathrm{N\Sigma K^+}$	2.62	-0.20
$\mathrm{NN} \rightarrow \mathrm{NNK^+K^-}$	2.86	-0.44
$\mathrm{NN} \rightarrow \mathrm{NN}\phi$	2.90	-0.48

Table 1.1: Possible production channels for hadrons containing strangeness with their threshold center-of-mass collision energy and the difference between this threshold and the available energy in measured Au + Au collisions.

Strangeness exchange reaction A strange quark from one hadron can be exchanged with light (u or d quark) from another hadron, and via this mechanism the threshold for some processes might be lowered but still at least some NN interaction must produce a strange hadron in the first place. An example of such a process is the reaction $\pi^-(d\bar{u}) + \Lambda(uds) \rightarrow \mathrm{K}^-(s\bar{u}) + \mathrm{n}(udd)$ [8].

In medium modification Due to the potential between the strange hadron and the nucleon, the effective mass of the strange hadron might be smaller than the nominal vacuum mass [9]. Several theoretical models [10–14] predict strong attractive $\mathrm{K^-N}$-potential compare to repulsive $\mathrm{K^+N}$-potential resulting in decrease of effective energy threshold for channel $\mathrm{NN} \rightarrow \mathrm{NNK^+K^-}$.

1.2 QCD application for HIC

The description of HIC is largely dependent on the energy scale [15]. In the case of large colliders (LHC and RHIC) where the transferred energy is large, the coupling constant of strong interaction α_s is decreasing, and this allows for a perturbative calculation of QCD. However, in the case of low-energy experiments (like fixed target experiments at SIS18), QCD becomes non-perturbative theory and the exact solutions are almost impossible. Luckily, at these low energies the hadronic processes are dominated by pions and the expansion of observables in terms of pion mass and momentum is possible, which is the principle of chiral perturbation theory (ChPT) [16]. Within these effective theories, which use the hadronic degrees of freedom (in contrast to quark and gluon degrees of freedom in QCD), a good characterization of interactions between pseudoscalar mesons and baryons can be deduced. A further reduction of the Lagrangian of ChPT to an effective Lagrangian where only some mesons and nucleons are used may be used to obtain a realistic picture of KN interactions. This way is very useful if one needs to avoid the coupled channel problem[3] which occurs when increasing numbers of particles are taken into account.

An important utilization of the above explained method with respect to the aim of this thesis is the production and propagation of strangeness in hot and

[3]For each species of particles, equation of motion is needed to solve separately, but due to interaction terms in Lagrangian these coupled equation create a complex problem.

dense nuclear matter. The first attempt to use a chiral Lagrangian for the description of kaon-nucleon interactions was made by Kaplan and Nelson [9, 17] and were followed by others [18–22]. Although it is possible to use a perturbative calculation on πN and KN interactions, $\bar{\mathrm{K}}$N is already too close to the threshold where resonances (like $\Lambda(1405)$) dominate. Therefore, the effective Lagrangian approach with mean field is preferable

$$\mathcal{L} = \bar{\mathrm{N}}(i\gamma^\mu\partial_\mu - m_\mathrm{N})\mathrm{N} + \partial^\mu\bar{\mathrm{K}}\partial_\mu\mathrm{K} - (m_\mathrm{K}^2 - \frac{\Sigma_\mathrm{KN}}{f_\pi^2}\bar{\mathrm{N}}\mathrm{N})\bar{\mathrm{K}}\mathrm{K} - \frac{3i}{8f_\pi^2}\bar{\mathrm{N}}\gamma^\mu\mathrm{N}\bar{\mathrm{K}}\overleftrightarrow{\partial_\mu}\mathrm{K}, \quad (1.3)$$

where $\mathrm{K} = (\mathrm{K}^+\ \mathrm{K}^0)$ and $\bar{\mathrm{K}} = (\mathrm{K}^-\ \bar{\mathrm{K}^0})$ are kaon field, $\mathrm{N} = (\mathrm{p}\ \mathrm{n})$ and $\bar{\mathrm{N}} = (\bar{\mathrm{p}}\ \bar{\mathrm{n}})$ are nucleon field, Σ_KN is kaon-nucleon sigma term [23]. The third term in the equation (1.3) comes from Kaplan and Nelson and is called the attractive scalar KN interaction term and the last term is Weinberg–Tomozawa [24, 25] and corresponds to the vector KN interaction which is found to be repulsive for kaons and attractive for antikaons. The sigma term can be expressed as the nucleon expectation value of Gell-Mann–Oakes–Renner equation ($m_\mathrm{K}^2 f_\mathrm{K}^2 \cong -1/2(m_u + m_s)\langle\bar{u}u + \bar{s}s\rangle$)

$$\Sigma_\mathrm{KN} = \frac{1}{2}(m_u + m_s)\langle\mathrm{N}\,|\bar{u}u + \bar{s}s|\,\mathrm{N}\rangle. \quad (1.4)$$

The in-medium kaon mass shift then can be evaluated as

$$m_\mathrm{K}^* \approx m_\mathrm{K}\left(1 - \frac{\Sigma_\mathrm{KN}}{m_\mathrm{K}^2 f_\mathrm{K}^2}\rho_S + \frac{3}{4}\frac{1}{m_\mathrm{K} f_\mathrm{K}^2}\rho_B\right), \quad (1.5)$$

where ρ_S and ρ_B are scalar and vector baryon density, respectively. The total strength of potentials can be compared to experiment V_KN from 20 to 30 MeV comes from K^+N scattering length and is in a good agreement, but for antikaons the predictions differ significantly due to the presence of $\Lambda(1405)$ resonance (the values of $V_{\bar{\mathrm{K}}\mathrm{N}}$ range from -50 to -200 MeV). As a result of the repulsive potential for kaons and the attractive potential for antikaons, the kaon condensation can occur in dense matter, e.g., in neutron stars. This would cause a softening of the equation of state and sequential reduction of the maximal neutron star mass to 1.5 solar masses (heavier stars would collapse into a black hole). Such a mass reduction contrasts with astronomical observations [26, 26] where neutron stars with 2 solar masses have been observed. Thus, new observables are needed to unravel this problem.

1.3 Motivation for this thesis

On the basis of the arguments stated above, the kaon (collective) flow might be a very useful tool for studying several important aspects of heavy-ion collisions. Already in the mid-1990s (relativistic HIC experiments started in the early 1970s) the kaon flow was suggested as a possible good probe of HIC [27]. The total kaon-nucleon cross section is small ($\sigma_\mathrm{KN} \approx 10$ mb) compared to the pion-nucleon cross section and therefore kaons are considered a good probe of the dense matter created at the early stage of HIC and of the kaon properties in compressed nuclear matter. It was shown in [28] that using the so-called azimuthal anisotropy

parameters

$$R_1 = \frac{N(90°) + N(270°)}{N(0°) + N(180°)} \quad R_2 = \frac{N(90°)}{N(180°)} \tag{1.6}$$

where $N(\Delta\phi)$ denotes the number of kaons that escape the collision with azimuthal angle $\Delta\phi = \phi_{\mathrm{K}} - \phi_{\mathrm{RP}}$ with respect to the reaction plane. Using the relativistic transport model (RVUU) calculation with Au + Au collisions at $1A\,\mathrm{GeV}$ and impact parameter $b = 3\,\mathrm{fm}$ they obtained kaon azimuthal distributions for two rapidity regions and for three scenarios: without any potential, with only vector potential and with scalar and vector potential. From these they calculated the azimuthal anisotropy parameters and showed them as a function of a strength of the potentials, see figure 1.1. The conclusion they made was that for the mid-rapidity region the sensitivity of R_1 is very small, but for the target rapidity the sensitivity increases significantly and therefore the kaon flow might serve as a useful probe of the kaon nucleon potential in dense matter. The influence of repulsive kaon nucleon potential reduces the flow (even induces an antiflow), with respect to the flow of nucleons, and the attractive antikaon nucleon potential would lead to similar flow to that of nucleons, however, the large $\mathrm{K}^-\mathrm{p}$ cross section leads to strangeness exchange reactions resulting in an almost isotropic emission pattern [29].

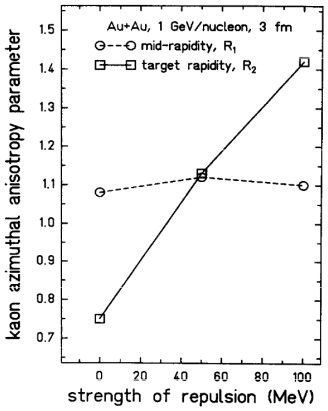

Figure 1.1: The azimuthal anisotropy parameters R_1 and R_2 as a function of the strength of KN repulsive potential. Taken from [28].

The first experimental results at both the SIS18 and AGS energies have shown almost zero flow, that is, the kaon average in-plane transverse momentum as a function of rapidity and its slope at mid-rapidity [30–32]. There were ideas on how to explain this vanishing kaon flow based on the isotropic production and canceling of the flow due to the production of kaons in the collision of hadrons with the opposite transverse flow. The theoretical calculations using transport models all predict that at the moment of creation, kaons have a positive initial transverse flow (inherited from nucleons), and this is later reduced because of the repulsive kaon potential in the nuclear medium. A quite surprising result was observed in the case of nucleon (proton) flow at incident energy, called the balance energy, where also vanishing flow was observed. However, it turned out using the so-called differential flow analysis [33] (split the measured interval of transverse momentum into smaller and investigate the flow within these intervals)

that there are two components: nucleons with high transverse momentum show positive flow and those with low p_T have negative flow.

Therefore, the differential approach for kaon flow is able to disentangle such effects and can bring more light to the problem of kaon properties in hot and dense matter. After the authors of [34] suggested, such an analysis was performed mainly in experiments with beam energies starting at several AGeV but seldom around the kaon production threshold energy (and never below). Due to the unprecedented statistics available in HADES gold beam time, such a measurement is possible for the first time.

1.3.1 Current experimental status of kaon flow at low energies

Due to the scare heavy-ion program at similarly low energies, the only relevant comparison is possible with experiments from GSI using SIS18 accelerator, namely, the experiments KaoS and FOPI. Very recently, STAR collaboration presented their results from fix-target experiment[4], and although the collision energy is still significantly higher than in presented analysis, in terms of system size (Au + Au) this is the closest measurement. Both GSI experiments are currently retired. They have measured many different systems (from light-ion to heavy-ion collisions) at several beam energies, which enabled them to obtain many important results on bulk properties. The published data on the kaon anisotropy of the azimuthal distribution w.r.t. reaction plane are usually integrated and differential analysis was solemnly performed and mainly for K^+. Flow of neutral kaons (K^0_S) is even more rare because of the need to reconstruct neutral kaons using their decay to charge pions.

Our up-to-date experimental knowledge on kaon flow in heavy-ion collisions is based on a very limited data set, see figures 1.2, 1.4, and 1.3. These published results are either for smaller systems slightly above the kaon production threshold or for the same system as presented in this thesis (Au+Au) but significantly higher collision energy. In summary, the results on K^+ show antiflow pattern at $p_T < 0.4\,\mathrm{GeV}/c$ changing to negative directed flow for higher transverse momenta. The results for neutral short-lived kaons reveal the same nature as positively charged kaons, while there are only weak indications of similar behaviour for K^-. All experiments observed perpendicular elliptic flow of K^+ with respect to reaction plane, the values of v_2 for K^- are mostly consistent with zero within error bars.

There has never been an analysis focusing on the subthreshold energy region, however, the importance of different undergoing processes is very much influenced by the energy region as well as the collision system size, e.g., probability of rescattering, multistep processes to produce strangeness. Thus, the presented, moreover, differential analysis of kaon flow including the comparison to different models predictions might shed some light on the topic of KN potentials and the properties of the equation of state of nuclear matter.

[4]Using a golden foil insert inside the beampipe they achieved a lower the collision energy compared to two-beam collider mode from $\sqrt{s_{NN}} = 7.7\,\mathrm{GeV}$ to $3.0\,\mathrm{GeV}$ [35].

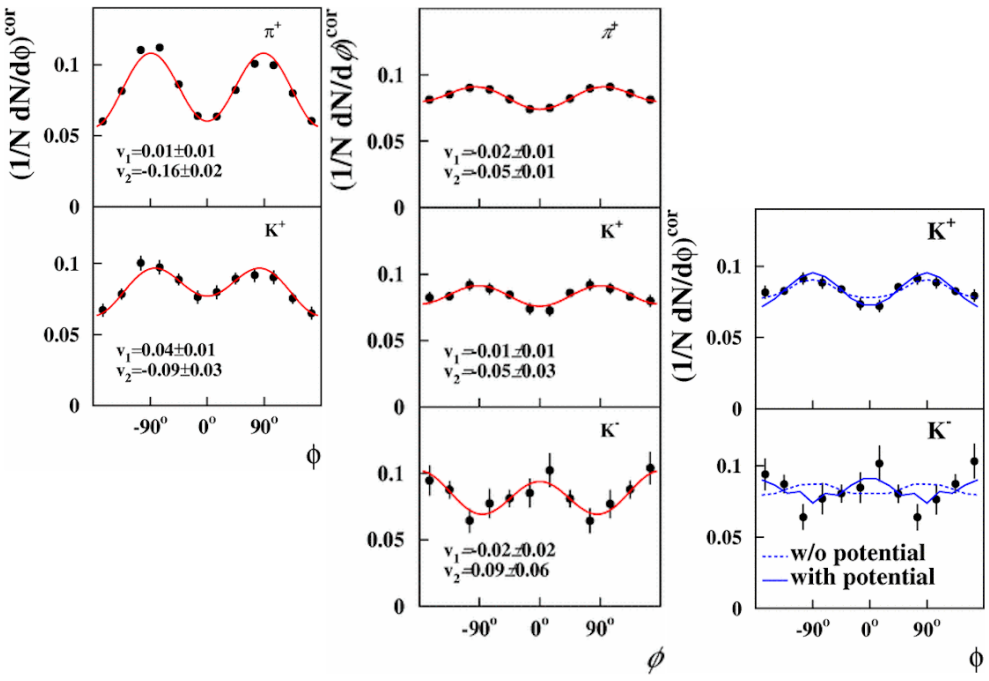

Figure 1.2: The azimuthal distributions of π^+ and charged kaons with respect to the reaction plane. On the left side are distributions from Au + Au collisions at $1.5A$ GeV, in the middle and on the right from Ni + Ni at $1.93A$ GeV. Two plots on the right side show results comparison with the IQMD model with and without KN and $\bar{\text{K}}$N potentials. Figures taken from [36].

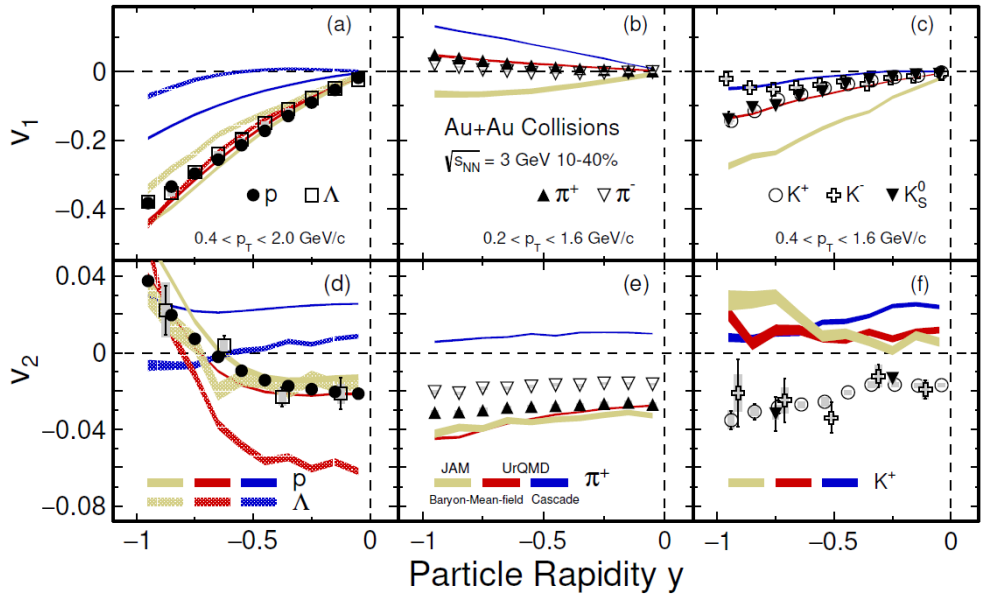

Figure 1.3: Directed and elliptic flow of protons, λ hyperons, pions, and kaons as a function of rapidity (integrated within given range of transverse momentum) measured by STAR collaboration in $10-40\%$ most central Au + Au collisions at $\sqrt{s_{\text{NN}}} = 3.0\,\text{GeV}$. The comparison to JAM and UrQMD models (both cascade and mean-field mode with incompressibility $\kappa = 380\,\text{MeV}$) is included for selected hadrons. Figure taken from [37].

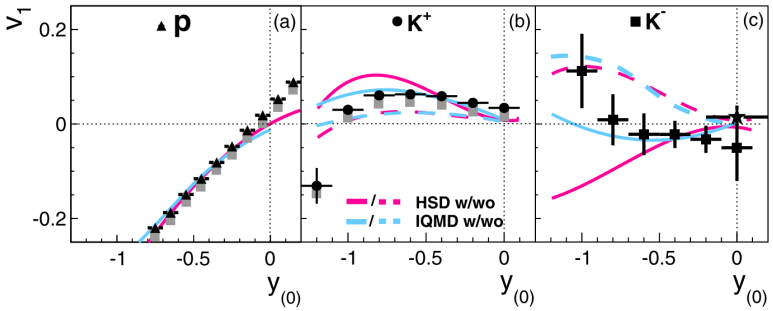

Directed flow of charged kaons and protons.

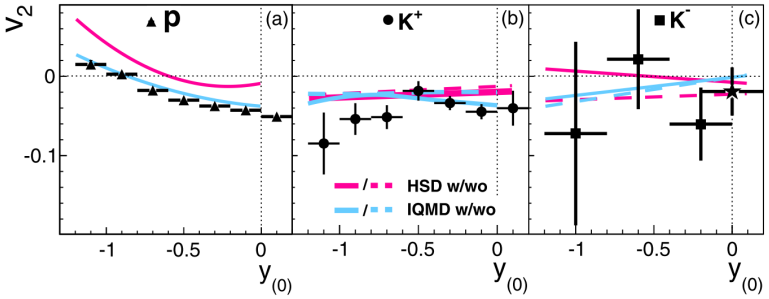

Elliptic flow of charged kaons and protons.

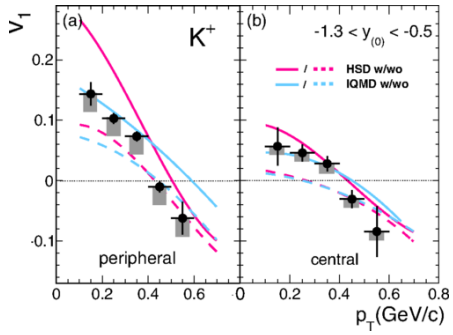

p_{T} differential directed flow of K^+.

Figure 1.4: Measurements of directed and elliptic flow from Ni + Ni collisions at 1.91A GeV beam kinetic energy for charged kaons and protons. Data are compared with simulation using HSD and IQMD models, both with and without inclusion of in-medium KN and $\bar{\mathrm{K}}$N potentials. Error bars (boxes) denote statistical (systematic) uncertainties. The star symbols for K^- mesons at mid-rapidity in (c) are from the high statistics data in the range $p < 1.0\,\mathrm{GeV}/c$ with $\frac{S}{B} > 5$. Figures taken from [38].

Chapter 2

HADES

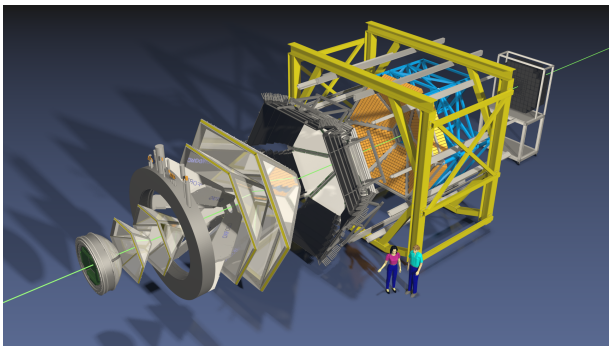

Recently, in 2019, the HADES collaboration celebrated already its 25$^{\text{th}}$ anniversary. This collaboration, consisting of 130 scientists from 20 institutes across Europe, has its roots at a *3*$^{\text{rd}}$ *workshop on real photon/dilepton program for SIS* where the results [39] from **D**i-**L**epton **S**pectrometer (DLS) located at Bevalac accelertor in Berkeley, California USA, were discussed and new a detector for the newly constructed accelerator SIS18 (**S**chwer**i**onens**y**nchrotron 18)[1] at GSI Helmholtzzentrum für Schwerionenforschung in Darmstadt, Germany, was proposed. The major improvements compared to the pioneering DLS experiment [41] were greater acceptance (85 % in azimuth angle and interval $18° < \theta < 85°$ in polar angle , more than 100-times larger)[2] and better mass resolution ($\delta m/m \approx 2\% \rightarrow$ 10-times smaller), see figure 2.1.

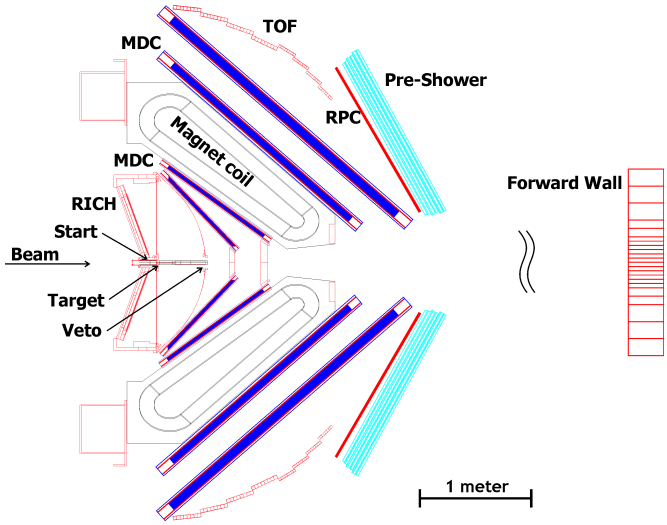

Figure 2.1: Cross-section of HADES spectrometer. Taken from [42].

In this short thesis version I will only briefly describe individual parts, much more details could be found in [43].

Target used during Au+Au experiment was segmented target to reduce the probability of interaction of produced particles with target material. The START

[1]Number 18 in the name of this heavy-ion synchrotron designate the bending power of installed magnets 18 Tm, the circumference of the accelerator is 216.72 m [40].

[2]From that comes the name HADES which means **H**igh-**A**cceptance **D**i**E**lectron **S**pectrometer.

and VETO detectors were diamond-based with gold coated strips. The time resolution of these detectors was around 50 ps. The **R**ing **I**maging **CH**erenkov detector is used to identify relativistic $e^{\pm}$ [44] and is supposed to be hadron-blind. For the tracking and momentum determination 4 planes of Multiwire Drift Chambers (MDC) and superconductiong magnet (creating toroidal magnetic field). The position resolution better than 150 μm is achieved resulting in the relative momentum resolution below 2%. To improve particle identification (not to be dependent only on energy loss and momentum from MDC) time measurement is used. This task is carried out by TOF (scintillator based time-of-flight detector) and RPC (resistive plate chambers) detectors. The time resolution of TOF detector is around 150 ps, in case of RPC 70 ps. In order to have good discrimination between electrons and pion even at higher momenta, Shower detector based on the detection of electromagnetic showers was present in HADES spectrometer. For the reconstruction of event plane, the scintillator based Forward hodoscope Wall is used during heavy-ion experiments. Reading out all information from already mentioned detectors simultaneously is the job of the **D**ata **A**c**Q**uisition system (DAQ). It consists of Front-End-Electronics boards (FEE), Trigger and Read-out Boards (TRB) and Event Builders (EB) that takes the correct data packages, put them together, and store them on discs and tapes.

Chapter 3

Event selection and track reconstruction

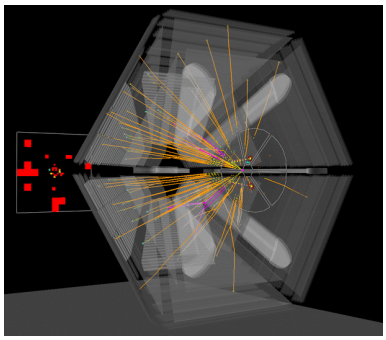

3.1 Beamtime overview

During two months (April and May) of 2012, the HADES experiment measured for the first time a heavy collision system. The kinetic energy of beam $^{197}_{79}\mathrm{Au}^{69+}$ gold ions was $E_{\mathrm{beam}} = 1.23\,A\mathrm{GeV}$ and the beam intensity provided by the SIS18 accelerator was $I_{\mathrm{beam}} = (1.2 - 1.5) \times 10^6\,\mathrm{s}^{-1}$. The target was segmented into 15 stripes of 25 μm thick circles with a diameter of 2.2 mm and separated by 4.5 mm.

The read-out trigger was based on the raw charged hit multiplicity in the TOF detector. The events were registered at an average trigger rate of 8 kHz with a duty cycle of 50 % and recorded on tape at a data rate of 200 MByte/s. After 557 hours of data taking, 7.31×10^9 events have been collected, from which 2.2×10^9 events were marked as good for further physics analysis (removed pile-up, interactions outside the target region, etc.).

3.2 Event selection and Centrality determination

If one wants to provide the highest quality measurements, the first thing to do is clean up the data sample. There are several sources which might be able to compromise our analysis, the main ones are pile-up events and interactions with other materials than gold target. The influence of each step of event selection on the number of entries is displayed on figure 3.1.

Since direct observation of the impact parameter (centrality of the collision) is impossible due to the high inelasticity of HIC at relativistic energies, indirect observables like the number of participating nucleons in the reaction N_{part} are linked to b via the Glauber model [4, 45]. Based on Glauber Monte Carlo simulations, one can calculate the averaged number of charged particles N_{ch} (which would in experiment transform to the number of TOF and RPC hits $N_{\mathrm{hits}}^{\mathrm{TOF+RPC}}$), additionally to allow event-by-event fluctuation around the averaged number of charged particles per participant nucleon is sampled by negative binomial probability distribution with mean value μ and dispersion parameter k thus we get

$\langle N_{\mathrm{ch}} \rangle = \mu \langle N_{\mathrm{part}} \rangle$. To take into account the non-linear response of the detector, the obtained distribution is further folded with a phenomenological efficiency function $\varepsilon(\alpha) = 1 - \alpha \cdot N_{\mathrm{part}}^2$. The simulated spectra are then compared to the measured one, and the intervals of $N_{\mathrm{TOF+RPC}}$ for centrality classes are introduced, see figure 3.1.

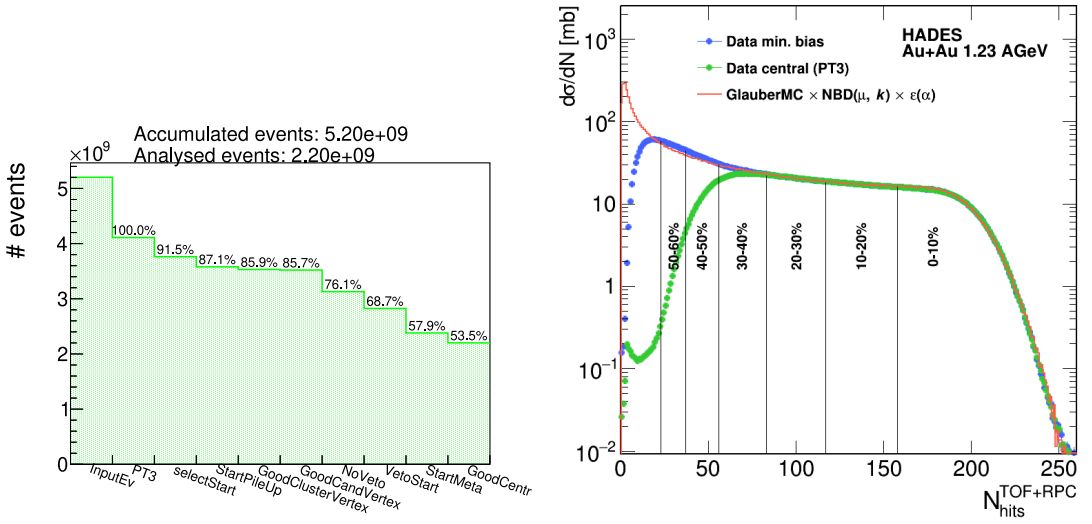

(a) (b)

Figure 3.1: (a) Histogram showing the number of events accepted after each step of event selection. This is already after the cleaning procedure of DST-files in which less than 5 sectors were stably operating. (b) Differential cross-section as a function of $N_{\mathrm{hits}}^{\mathrm{TOF+RPC}}$. Comparison between minimum bias (blue), PT3 trigger (green), and weighted simulated Glauber model spectra is shown (figure taken from [46]).

3.3 Track reconstruction

The tracking algorithm used for charged particles that pass through HADES spectrometer is rather complex and complicated, and thus only a short introduction will be given here. A nice overview of the algorithm is displayed in figure 3.2. We will try to outline the individual steps below. The underlying physical principle of particle detection is the ionization of gas inside MDC chambers. After the drifting electrons are registered on the sense wire, we call it the fired wire.

The starting point is to determine inside which segment of the gold target the interaction most likely occurred. For that purpose, the Cluster Vertex Finder is called, and the fired wires are projected to each target segment and the one with the best projection resolution is further used as a reaction vertex. To find the position of the tracks, we define common planes (one for two inner MDCs and one for two outer MDCs), and all fired wires from both chambers are projected to that plane. Then we can observe a local maxima on the crossing of the fired wires where the particle went through. To define the inner segment of the track, we use these true clusters and the reaction vertices connected by a straight line. This line is prolonged to the so-called kick plane, which is located in the region

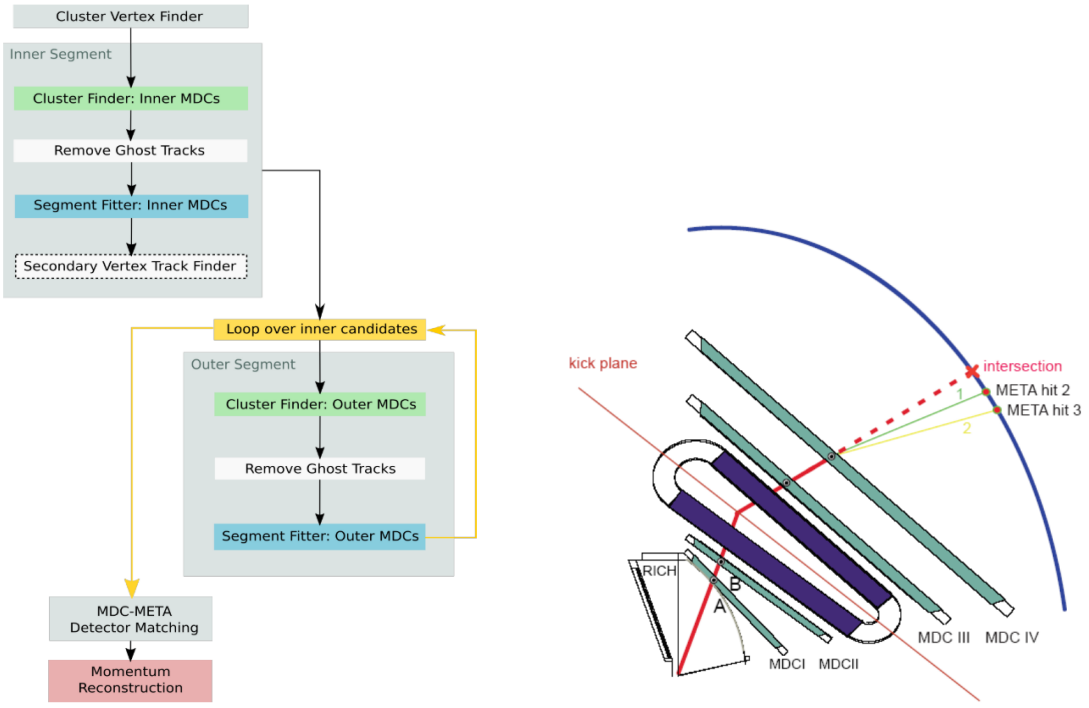

(a) (b)

Figure 3.2: (a) Flow chart of track reconstruction with individual steps specified in the text. (b) Sketch of META matching. Figures taken from [47, 48].

of maximum magnetic field. The intersection is then used as a starting point of a line that goes through the true clusters of the second common plane between the MDC III and IV. However, the number of wrongly fired wires due to the noise and questionable cluster assignment can be very significant (about 50 %), and removal of such false segments (ghost tracks) is necessary. A fairly new feature of the tracking algorithm is the secondary vertex track finder. In this procedure, the tracking algorithm takes a look at the fired wires that are not used in the fitted inner segments, connects them with a line, and tries to find other fired wires around this line. If at least 7 such wires are found, then the connected line is fitted to the drift cell as described above, and such a segment is added to the list of reconstructed inner segments with a special off-vertex flag. This procedure increases the number of reconstructed weakly decaying particles like K^0_S by more than 10 %.

The momentum determination is achieved using the so-called Runge-Kutta method, which is a technique used to obtain an approximate numerical solution of differential equations (in this case the equation of motion). The resulting momentum p and initial direction are stored in DST files together with a specific χ^2_{RK} value (the sum of squared differences between RK fit and the actual position of MDC hits weighted with errors of the positions - these are in some cases rather small causing large χ^2) which is later used as the track quality criterion.

By extrapolation of the outer segments to the META detector, we get an idealized position of the META hit, see figure 3.2. Matching to a fired META hit is done based on the difference in the y-direction (which is preferred over x due to the natural geometry of META cells), where the maximal difference is a

momentum-dependent value up to 4 mm for high-momentum tracks.

3.4 Particle identification

3.4.1 Charged particle identification

Long-lived charged particles are being identified either by time-of-flight and momentum measurements or via specific energy losses.

Identification based on time-of-flight and momentum measurement

Thanks to the Runge-Kutta track fitting, we have a good understanding of the length of the particle trajectory s and its direction of bending in the magnetic field. During the Au + Au experiment, the magnetic field forced the positive particles to bend in and negative out of the direction of the beam axis. Joined with the time-of-flight $\Delta t = t_1 - t_0$, using START time t_0 and META hit time t_1, this provides us information about the velocity of the particle

$$\beta = \frac{v}{c} = \frac{s}{c\Delta t}. \tag{3.1}$$

The measured particle's velocity versus momentum divided by its charge is displayed on figure 3.3. Due to the difference in time resolution, the TOF and RPC detectors are shown separately.

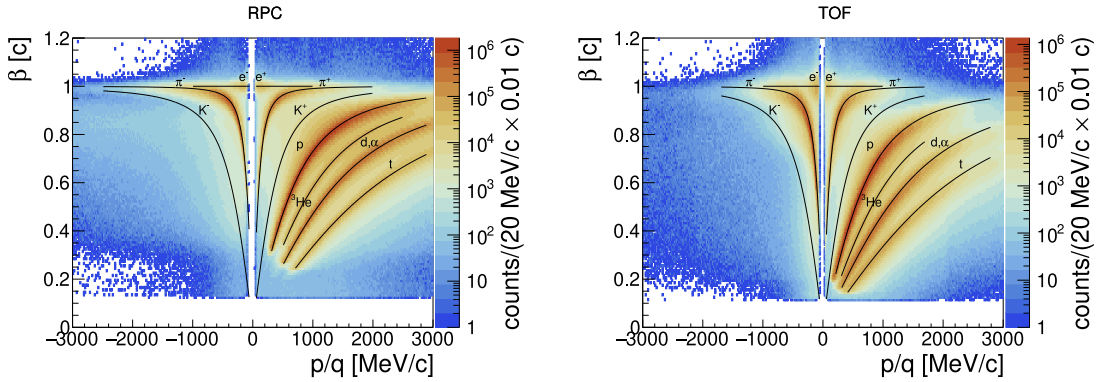

Figure 3.3: Measured correlations of velocity and momenta scaled by particle's charge in Au + Au collisions at $E_{\mathrm{kin}} = 1.23A\,\mathrm{GeV}$, using RPC and TOF detector for time-of-flight measurement on the left and right side, respectively.

Identification via specific energy loss

The second method used for charge particle identification uses the specific energy loss per unit path length in MDC and TOF detectors. The mean energy loss per unit path length is prescribed by the Bethe equation. For the range of momenta accepted by the HADES spectrometer and the masses of charged particles created in HIC at SIS18 energy, the Bethe equation gives proper predictions as can be seen from figure 3.4, where the measured energy losses within MDC and TOF from the experiment are compared with the model predictions from the Bethe equation.

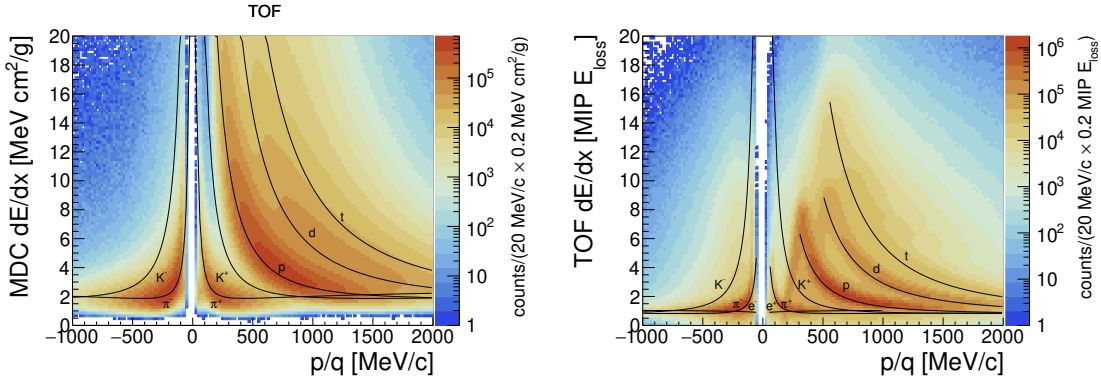

(a) (b)

Figure 3.4: (a) Measured correlations of energy losses within the MDC detector and momenta scaled by particle charge. (b) Measured correlations of energy losses within the TOF detector and momenta scaled by particle charge.

3.4.2 Decaying particle identification

When the daughter particles are identified, they can be combined, and using the four-momentum algebra, the invariant mass of the mother particle might be calculated (for simplicity, we will present here only the case of two particles which is also the analysed case of K^0_S in this thesis). The nominal masses m_i of the daughter particle species, taken from [6], are assigned to the reconstructed and identified tracks and together with their momentum $\vec{p}_i$ from Runge-Kutta method gives us the desired invariant mass

$$M^2_{\text{inv}} = m_1^2 + m_2^2 + 2\sqrt{m_1^2 + p_1^2}\sqrt{m_2^2 + p_2^2} - 2p_1p_2\cos\Delta\omega_{12}, \tag{3.2}$$

where $\Delta\omega_{12}$ is the opening angle between the daughter particle tracks.

Background

There are usually many possible combinations of the charged decay products (in the case of $K^0_S \to \pi^+\pi^-$ coming from Au + Au collisions at $\sqrt{s_{NN}} = 2.42\,\text{GeV}$ on average there are 7 π^- and 4 π^+ [49], i.e. 28 combinations) resulting in the so-called combinatorial background. In the spectrum of invariant mass, there are four sources [50]:

Signal selected tracks come from one decay of the particle of our interest, their invariant mass would be around the nominal mass of the mother (smearing due to finite spectrometer resolution and width of the decayed particle is expected).

Uncorrelated background selected tracks do not have a common mother particle, therefore, their invariant mass is defined by the phase space and the HADES acceptance.

Correlated background selected tracks originate from one decay but not the particle that we intend to study (e.g., Λ or $\Delta^0(1232) \to p\pi^-$).

Misidentification one of the selected tracks was misidentified, e.g., in reality it was a proton but due to incorrect META matching was labeled as π^+.

The challenge of a perfect description of the background is of utter importance, because if it is successful, then the pure signal would be left and the precise results of physics analysis would be obtained. A powerful method for background estimation is the **Mixed-Event technique**. As the title suggests, it combines the daughter particles of one kind from one event with the daughter particles of a second kind from another event, finally providing us good description of the uncorrelated background.

3.5 Simulations

In addition to real experimental data, it is needed to analyse in the same way also Monte Carlo (MC) simulations. The scheme of the entire analysis procedure is shown in figure 3.5. The necessity of MC simulations comes from the inaccessibility of some physical variables in the experiment, e.g., impact parameter, or the evaluation might be too complicated due to the entanglement between different components of the spectrometer, e.g. detection efficiency.

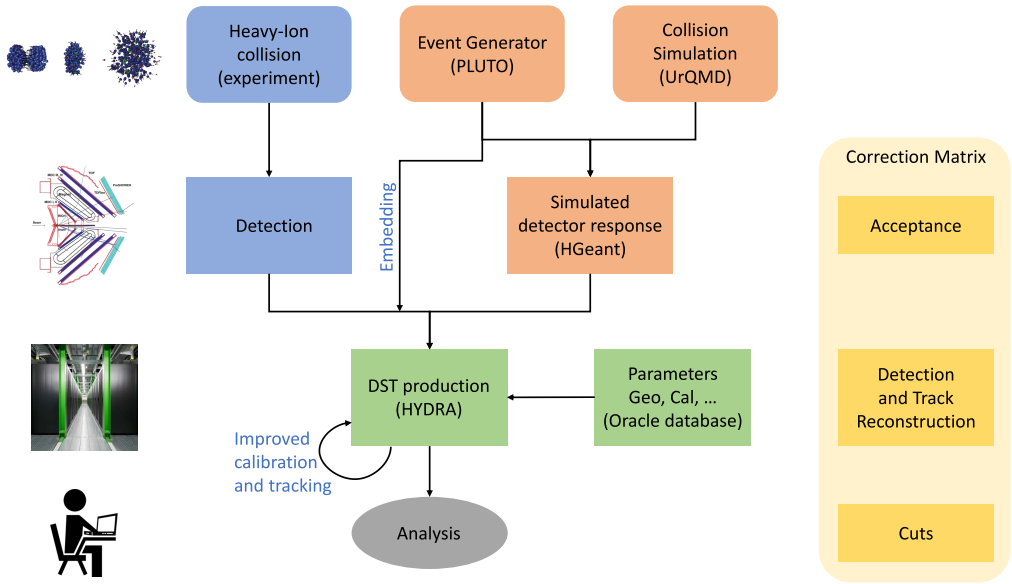

Figure 3.5: Flow chart of the analysis scheme showing individual steps and required tools. At each step, separate parts of the correction matrix are displayed.

Chapter 4

Kaon reconstruction

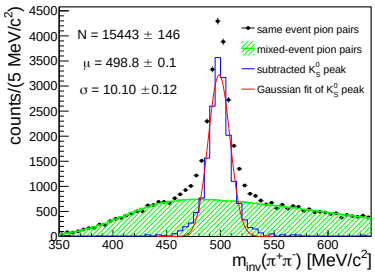

4.1 Charged kaons

Each detected charged particle and its reconstructed track obtain the calculated mass. Since kaons are rarely produced in analysed HICs at subthreshold energy, it is necessary to make additional selection criteria, in order to get better signal-to-background ratio of kaon peak in the mass spectra. Due to the fact that charged kaons are sitting on the non-Gaussian tails of surrounding particles it is desirable to apply strong cuts on the track quality parameters χ^2_{RK} and χ^2_{MM}. In addition to that, specific energy losses inside the MDC (reducing proton and pion background) and TOF (using as veto cut, further reducing background coming from incorrectly combined proton velocity with pion track momentum) are used. The summary table with the selection criteria used is in table 4.1, and their performance on background reduction is visible on figure 4.1.

variable	criteria
χ^2_{RK}	< 100
χ^2_{MM}	< 2
$\mathrm{d}E/\mathrm{d}x$ in MDC	graphical cut
$\mathrm{d}E/\mathrm{d}x$ in TOF	graphical veto cut

Table 4.1: Summary of selection criteria used for charged kaon identification.

Even after careful track selection, we can observe significant background contamination in the mass spectra shown in figure 4.1. Its subtraction is a decisive step in the present analysis. The cubic polynomial function was selected as the best candidate for background description together with the Gaussian function for the kaon peak of the mass spectra. Because of the importance of this step for flow analysis, careful check of the fit parameters, as well as eye inspection, was used to avoid any obvious errors.

After the above mentioned steps are performed, we can make the charged-kaon phase space distribution which is displayed in figure 4.3 together with the signal-to-background ratio of the kaon mass peak.

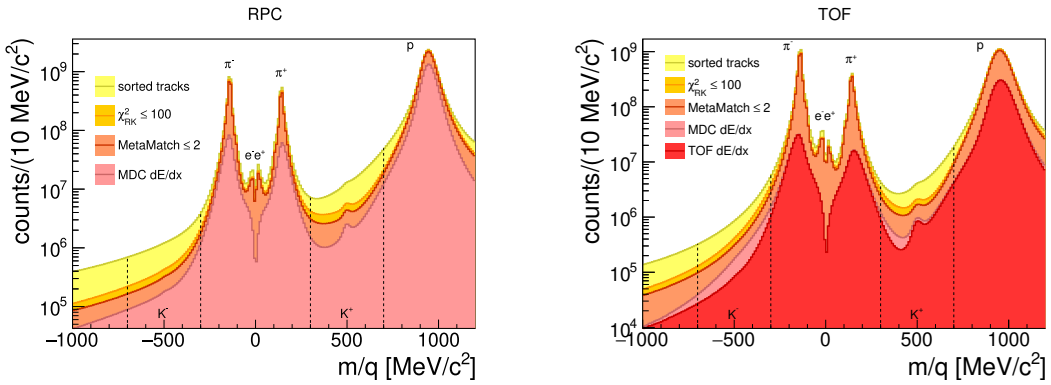

Figure 4.1: Measured spectra of mass scaled by particle's charge in Au + Au collisions at $E_{\text{kin}} = 1.23A\,\text{GeV}$ with selection criteria applied in steps (only region important for charged kaon identification is shown), using RPC and TOF detector for time-of-flight measurement on the left and right sides, respectively.

4.2 Neutral kaons

As one of the weakly decaying strange hadrons, neutral kaons live sufficiently long enough to escape from the fireball created in HIC and decay far enough from its spatial point of origin to allow us to distinguish between these two vertices. In the following we will try to introduce a procedure of selection of the pion pairs with high probability to originate from the neutral kaon decay. The summary table with the selection criteria used is in table 4.2.

variable	criteria
χ^2_{RK} for both π^+ and π^-	< 400
χ^2_{MM} for both π^+ and π^-	< 3
$\left\lvert\frac{m}{q}\right\rvert$	> 0 and $< 300\,\text{MeV}/c^2$
topology precuts	defined in (4.1)
$\Omega_{\text{MLP}}\,(d_1, d_2, d_3, d_{\text{ver}}, d_{\text{min}}, p_{\text{mother}})$	> 0.975

Table 4.2: Summary of selection criteria used for neutral kaon identification.

Due to high number of combinatorial background of pion pairs and low production probability of neutral kaons, we must introduce the so-called topology cuts, i.e., a set of limitations for the variables: d_1 and d_2 are the minimal distances of charged pion tracks to the event vertex (also referred to as global vertex); d_3 is the minimal distance of the combined track of the charged pion pair to the event vertex; d_{ver} is the distance between the event vertex and point where the two charged pion tracks are closest to each other (the so-called decay vertex); d_{min} is the minimal distance between the two charged pion tracks.

The power of topology cuts can be seen from figure 4.2, where the invariant mass spectra of charged pion pairs from the same event are displayed using different topology selection criteria. Although it is possible to define cuts on variables d_{x} so-called by hand, a much better way is to use dedicated tools for such optimization tasks as TMVA [51]. However, it is very difficult for the algorithm (we

used supervised learning of MLP NN with simulated K^0_S tracks embedded into real data) to search for such a hidden signal as neutral kaons, therefore, a set of precuts for d_x variables were introduced to decrease the number of pion pair combinations, see figure 4.2. The values implemented in the present analysis are

$$d_1 > 6\,\text{mm}, \quad d_2 > 6\,\text{mm}, \quad d_3 < 12\,\text{mm}, \quad d_{\text{ver}} > 17\,\text{mm}, \quad d_{\text{min}} < 13\,\text{mm}. \tag{4.1}$$

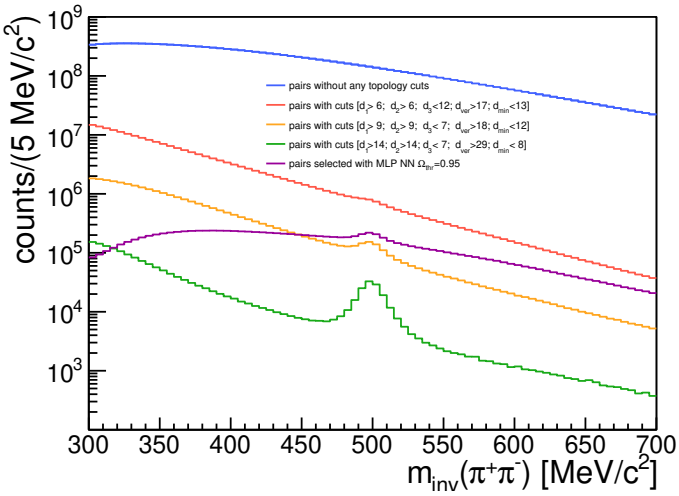

Figure 4.2: Invariant mass spectrum of charged pion pairs for multiple sets of topology cuts: the black line shows the spectra for all possible combinations (no cuts), the blue lines correspond to the topology precuts defined in (4.1), green line refers to cuts optimized for $S/\sqrt{S+B}$, red line is for a very high S/B ratio, and the purple line spectra was obtained with MLP NN.

For remaining background (mostly from uncorrelated pairs) the Mixed-Event technique is used with very good results.

K^0_S phase space distribution, shown in figure 4.4 together with the signal-to-background ratio of the kaon mass peak, immediately points out that due to smaller statistics, the flow analysis of the neutral kaon would suffer from large uncertainties. However, in comparison to K^- we observe much larger S/B ratios which give us a better chance for differential flow analysis.

4.3 Acceptance and Reconstruction Efficiencies

Using the so-called embedding technique (inserting simulated track into real data) one has a control of the individual steps in the track reconstruction and particle identification, and at the same time keeping the simulations as close to real data as possible. Since we know the number of embedded tracks N_{input} and their phase space distribution, we can compare it to the number of accepted tracks N_{acc} (we ask that the simulated track has at least 4 hits in each MDC plane and one META hit)

$$\varepsilon_{\text{acc}}(y_{(0)}, p_{\text{T}}, \mathcal{C}) = \frac{N_{\text{acc}}}{N_{\text{input}}}, \tag{4.2}$$

where we define the acceptance $\varepsilon_{\text{acc}}(y_{(0)}, p_{\text{T}}, \mathcal{C})$ dependent on the phase space variables and the centrality of the event $\mathcal{C}$. Similarly, the reconstruction efficiency,

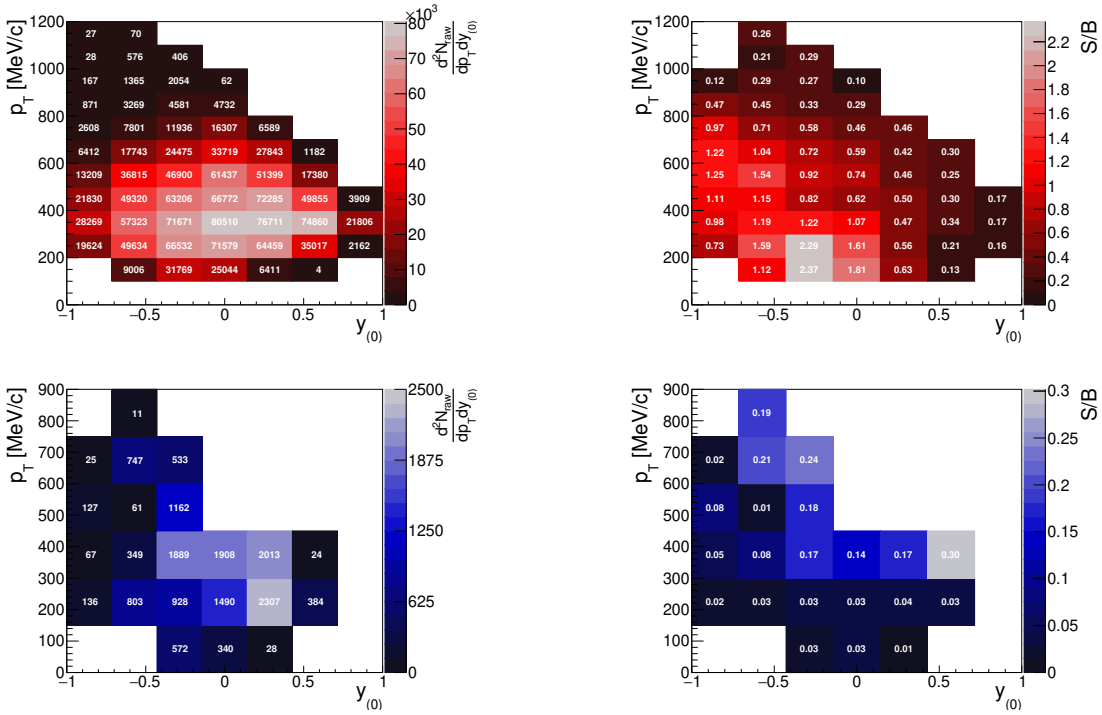

Figure 4.3: Charged kaon phase space distribution and signal-to-background ration of the kaon peak in mass spectra in $20\% - 30\%$ most central collisions. Upper row is for K^+, lower for K^-.

which covers all effects originating from the tracking algorithm and selection criteria (track quality, energy loss, topology cut, etc.), is determined as

$$\varepsilon_{\text{reco}}(y_{(0)}, p_{\text{T}}, \mathcal{C}) = \frac{N_{\text{reco}}}{N_{\text{acc}}}, \tag{4.3}$$

where N_{reco} is the number of reconstructed and selected kaon tracks (the same analysis code is used for simulations as for the measured data). In the case of $20\% - 30\%$ the most central collisions, the acceptance and reconstruction efficiencies for charged and neutral kaons are depicted in figures 4.5,4.6 and 4.7.

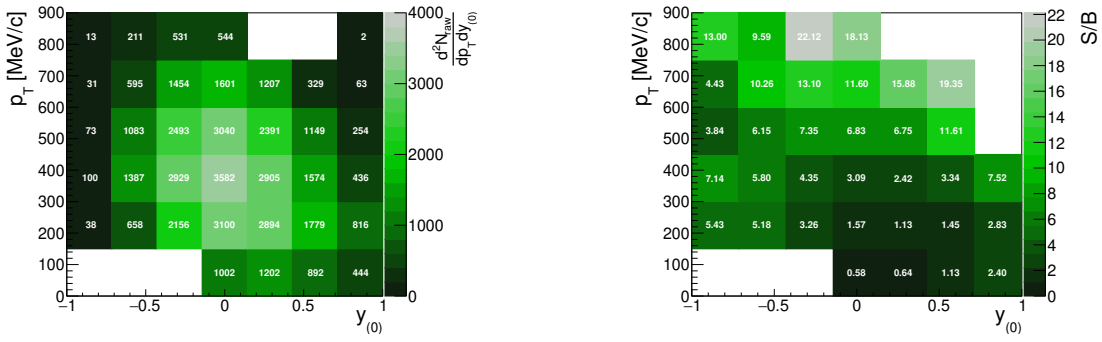

Figure 4.4: Neutral kaon phase space distribution and signal-to-background ration of the kaon peak in mass spectra in $20\% - 30\%$ most central collisions.

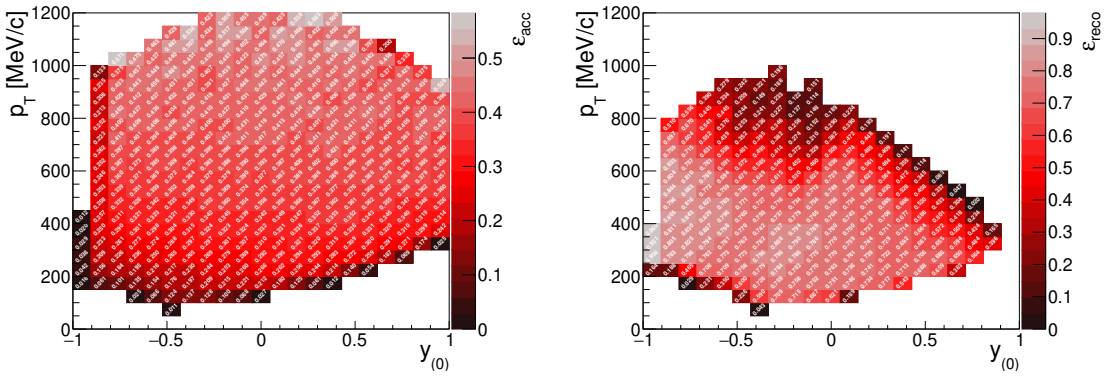

(a) (b)

Figure 4.5: K^+ acceptance in (a) and reconstruction efficiency in (b) for $20-30\,\%$ centrality class.

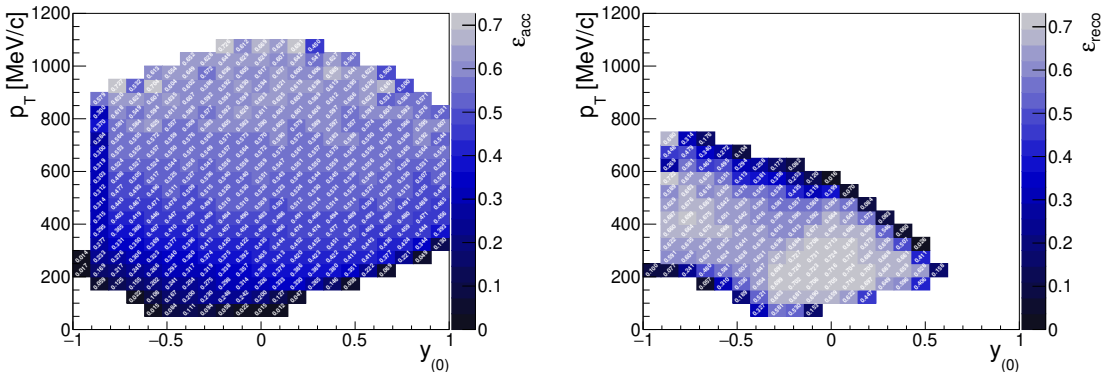

(a) (b)

Figure 4.6: K^- acceptance in (a) and reconstruction efficiency in (b) for $20-30\,\%$ centrality class.

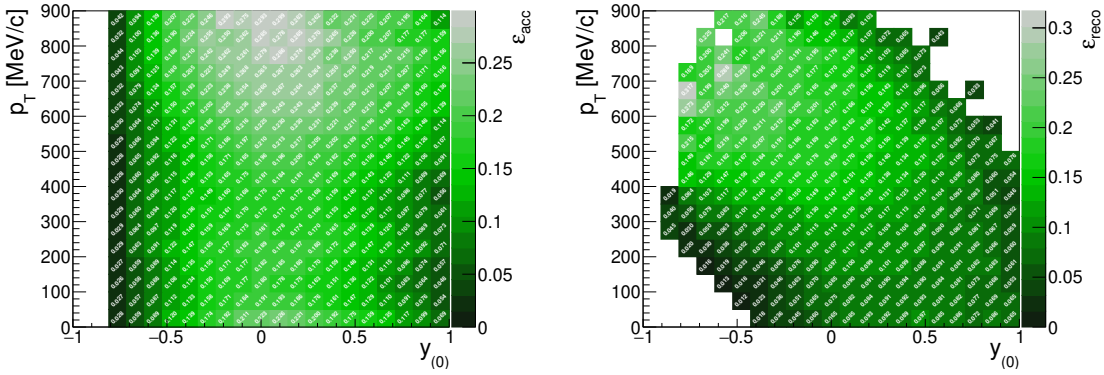

(a) (b)

Figure 4.7: K^0_S acceptance in (a) and reconstruction efficiency in (b) for $20-30\,\%$ centrality class.

Chapter 5

Measurement of collective flow

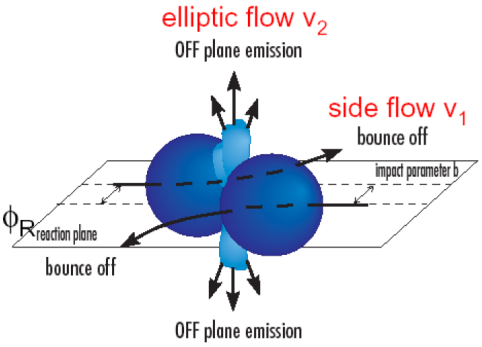

5.1 Standard flow method

The method published in the article of Poskanzer and Voloshin [52] would be summarised, and its actual application for HADES will be given in detail. The method presented is divided into several steps: the first is reaction plane estimation (so-called event plane), evaluation of Fourier coefficients in the expansion of the azimuthal distribution of particles with respect to the event plane, correction of these coefficients for the finite number of detected particles (division by the event plane resolution, which is estimated using the sub-event method).

5.1.1 Estimation of reaction plane

In case of differential flow analysis we study triple differential distribution

$$E\frac{\mathrm{d}^3N}{\mathrm{d}p^3} = \frac{1}{2\pi}\frac{\mathrm{d}^2N}{p_\mathrm{T}\mathrm{d}p_\mathrm{T}\mathrm{d}y}\left(1+\sum_{n=1}^{\infty}2v_n\left(p_\mathrm{T},y\right)\cos\left[n(\phi-\Psi_\mathrm{RP})\right]\right), \tag{5.1}$$

where Ψ_RP is the azimuthal angle of the reaction plane, and the Fourier coefficients v_n are easy to interpret as $v_n = \langle\cos\left[n(\phi-\Psi_\mathrm{RP})\right]\rangle$ where the brackets represent averaging over all particles in all events. As the reaction plane is not accessible in the experiment (since the actual vector of impact parameter is unknown), we must use only estimates of Ψ_RP. These estimates are usually called event planes, and for their determination the anisotropic flow is used. The event flow vector Q_n and the event plane angle Ψ_n is calculated for each harmonic independently using a set of equations

$$Q_n\cos(n\Psi_n) \quad = X_n \quad = \sum_i \omega_i\cos(n\phi_i), \tag{5.2}$$

$$Q_n\sin(n\Psi_n) \quad = Y_n \quad = \sum_i \omega_i\sin(n\phi_i), \tag{5.3}$$

where we might select only some particles i with weights ω_i for the event plane determination. The selection of particles, which we use to determine the event plane, and particles whose anisotropic flow is under study, might lead to autocorrelations. In most of the experiments this effect is avoided with (pseudo-)rapidity

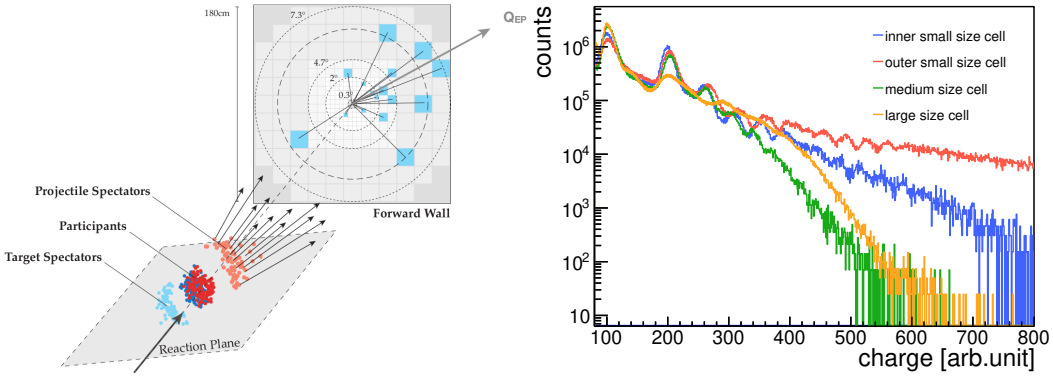

Figure 5.1: (a) Sketch of event plane determination used by HADES collaboration [42] (Credit: B. Kardan). (b) Fragment charge distribution in different Forward Wall cells.

separation of these sets of particles. In case of HADES the Forward-Wall (FW) detector is used for event plane determination. It detects projectile spectators, mostly protons and light ions, and their charge is used as weight $\omega_i = |Z_i|$.

5.1.2 Fourier decomposition with respect to Ψ_n

One can study the Fourier coefficients v_n using any harmonic m of the reaction plane estimation if $n \geq m$, and n must be a multiple of m, e.g. Ψ_1 can be used for any v_n, Ψ_2 only for even n, Ψ_3 for $v_{3,6,\ldots}$, etc. The Fourier decomposition from (5.1) thus changes to

$$\frac{\mathrm{d}(wN)}{\mathrm{d}(\phi - \Psi_m)} = \frac{\langle wN \rangle}{2\pi} \left(1 + \sum_{k=1}^{\infty} 2v_{km}^{\mathrm{obs}} \cos\left[km(\phi - \Psi_m)\right] \right), \tag{5.4}$$

where the general weights w are equal to p_T in the case of transverse momentum flow analysis, but could also be unity for the study of flow of a number of particles. In HADES case we are using only the first harmonic Ψ_1 as event plane for all v_n because at rather low energy HIC the multiplicity of particles is much smaller compared to experiments at RHIC and LHC, and the Fourier coefficients for higher harmonics are small too, see [53, 54].

The coefficients $v_n^{\mathrm{obs}} = \langle \cos\left[n(\phi - \Psi_m)\right]$ are always smaller than the true v_n, implying the necessity of the so-called event plane resolution correction

$$v_n = \frac{v_n^{\mathrm{obs}}}{\langle \cos\left[km(\Psi_m - \Psi_{\mathrm{RP}})\right] \rangle}. \tag{5.5}$$

5.1.3 Event plane resolution

The event plane resolution $\langle \cos\left[km(\Psi_m - \Psi_{\mathrm{RP}})\right] \rangle$ depends on the harmonic m used for event plane determination as well as on the order n of Fourier coefficients. In [55] the authors derived a formula for EP resolution

$$\langle \cos\left[km(\Psi_m - \Psi_{\mathrm{RP}})\right] \rangle = \frac{\sqrt{\pi}}{2\sqrt{2}} \chi_m \exp(-\chi_m^2/4) \left[I_{\frac{k-1}{2}}(\chi_m^2/4) + I_{\frac{k+1}{2}}(\chi_m^2/4) \right], \tag{5.6}$$

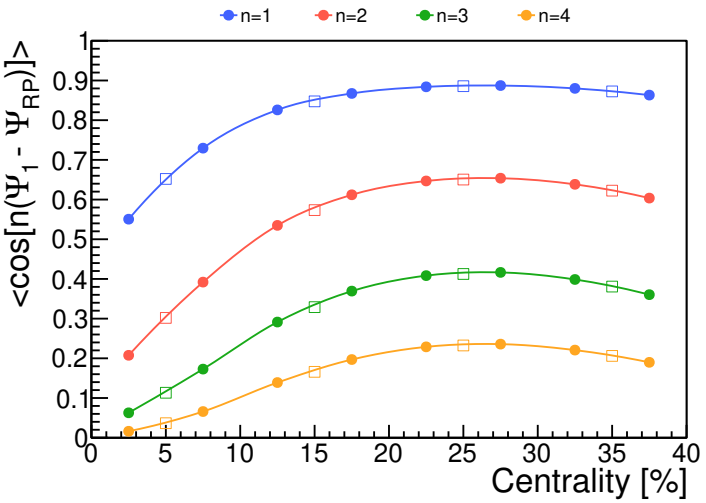

Figure 5.2: Event plane resolution $\langle \cos\left[n(\Psi_1 - \Psi_{\mathrm{RP}})\right]\rangle$ for different harmonics of Fourier decomposition as a function of centrality. Full circles are for 5% and open squares for 10% centrality classes, lines are only to guide the eyes.

where $\chi_m \equiv v_m/\sigma$ (where $\sigma^2 = \frac{1}{2M}(\langle w^2\rangle/\langle w\rangle^2)$ and M is the number of particles used for event plane determination) and I_ν is the modified Bessel function of order ν.

To overcome the inaccessibility of the reaction plane in experiments, two independent sets a, b of particles (either from different phase space windows or a random distribution of the so-called sub-events introduced in [56]). From trigonometry one easily deduces

$$\begin{aligned} \langle \cos\left[n(\Psi_m^a - \Psi_m^b)\right]\rangle = \langle \cos\left[n(\Psi_m^a - \Psi_{\mathrm{RP}})\right]\rangle \times \langle \cos\left[n(\Psi_m^b - \Psi_{\mathrm{RP}})\right]\rangle \Rightarrow \\ \Rightarrow \langle \cos\left[km(\Psi_m - \Psi_{\mathrm{RP}})\right]\rangle = \sqrt{2\langle \cos\left[km(\Psi_m^a - \Psi_m^b)\right]\rangle}, \end{aligned} \tag{5.7}$$

where the factor of 2 under the square root comes from the fact that the number of particles in sub-events is $M/2$ and the χ_m is proportional to $\sqrt{M}$.

If $\chi_m < 2.5$ the approximate equation $N\left(m\left|\Psi_m^a - \Psi_m^b\right| > \pi/2\right)/N_{\mathrm{total}} = \exp(-\chi_m^2/4)/2$ introduced in [57] can be used for evaluation of χ_m, which is afterwards inserted into (5.6), and the EP resolution is obtained, see figure 5.2 for the actual values calculated for analyzed data set.

5.1.4 Occupancy corrections

The actual efficiency of track reconstruction in central collisions is decreasing with the impact on flow measurement due to the higher concentration of tracks around the reaction plane[1]. The density of tracks per event and 1 cm^2 at a distance of 2 m from the target is displayed on figure 5.3 separately for each centrality class but keeping the same scale of the color axis. It is obvious from the figures that due to

[1]The origin of the loss of tracks lies in the ambiguity of the assignment of firing drift cells to a given track. Within a certain cut window, the tracking algorithm is not able to distinguish between two tracks within a very small space-time window.

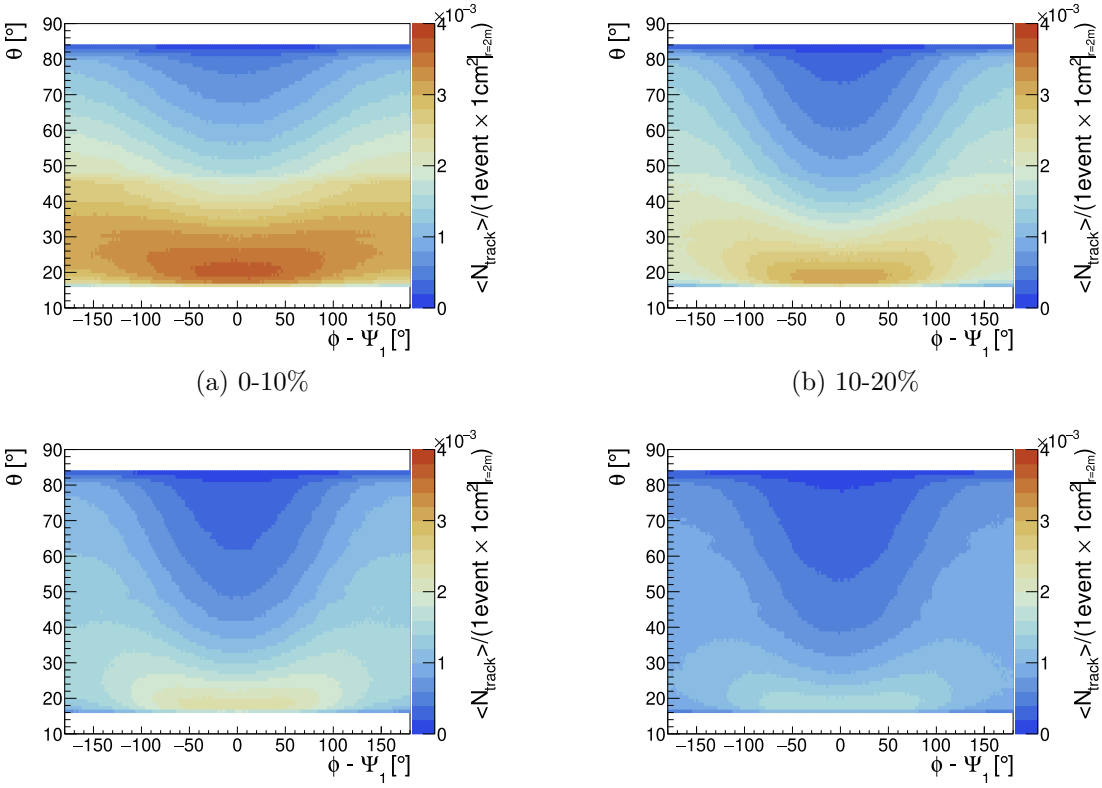

(a) 0-10%

(b) 10-20%

(c) 20-30%

(d) 30-40%

Figure 5.3: Distribution of track density for each analysed centrality class as a function of polar angle θ and azimuthal angle difference with respect to event plane angle $\phi - \Psi_1$.

the higher density of tracks close to the azimuthal angle of the event plane (which we use as an approximation to the true inaccessible reaction plane angle), and for lower polar angles the effect on the measured tracks will differ significantly. It should be mentioned that this is not a problem of HADES spectrometer alone, but similar corrections were implemented in other experiments too, e.g. FOPI [58] and PHOBOS [59].

The effect of track density around a particular track of interest was studied using the HGeant simulations, however, the obtained corrections were not able to fully compensate the observed effect. Thus, a data-driven approach was developed using an assumption of a linear or quadratic dependency of the track reconstruction efficiency on the track density $\langle \rho_{\text{track}} \rangle = N_{\text{track}}/(1\,\text{event} \times 1\,\text{cm}^2|_{r=2m})$

$$\varepsilon_{\text{occup}}(\langle \rho_{\text{track}} \rangle) = \varepsilon_{\text{max}} - C(\langle \rho_{\text{track}} \rangle - \rho_0)^{1 \text{ or } 2}, \tag{5.8}$$

where we know from the simulations that for $\langle \rho_{\text{track}} \rangle < \rho_0$ there is no decrease of efficiency due to track density and therefore $\varepsilon_{\text{occup}} = \varepsilon_{\text{max}}$. The values $\rho_0 = 7.\times 10^{-4}$ and $\varepsilon_{\text{max}} = 0.98$ were obtained from simulations. Due to different dynamics of each particle species, these corrections have to be also particle dependent and thus the value of constant C has to adjusted respectively (pions [42, 60], electrons [61], protons [42] and Lambda hyperons [62]). The functional dependence of the applied corrections for selected particle species is shown on figure 5.4. For decaying particles like K^0_S and Λ the efficiency is calculated as a multiple of the

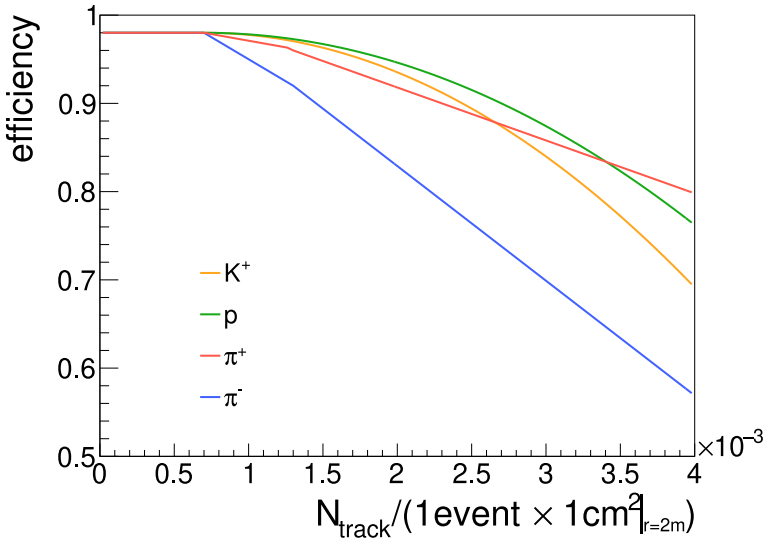

Figure 5.4: Functional dependence $\varepsilon_{\text{occup}}(\langle\rho_{\text{track}}\rangle)$ for selected particle species.

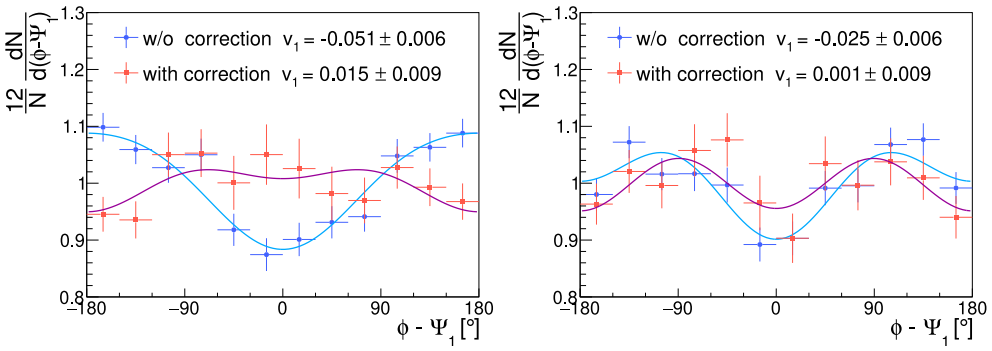

(a) 0-10% (b) 20-30%

Figure 5.5: Positively charged kaon azimuthal angle distribution w.r.t. event plane with and without the occupancy corrections for the midrapidity bin ($y_{(0)} \in (-0.14; 0.14)$) and low transverse momenta ($p_{\text{T}} \in (200; 300)\,\text{MeV}/c$). These values correspond to $\theta \approx 30°$ through an equation $\tan^2\theta = p_{\text{T}}^2 / \left[\sinh^2 y\,(p_{\text{T}}^2 + m^2)\right]$.

efficiencies of the decay products.

The requirement given for the determination of a constant C is the symmetry of directed flow expressed in the form of $v_1(\mathcal{C}, p_{\text{T}}, y_{(0)} = 0) = 0$. This ideal state is, however, difficult to achieve with just one parameter, thus we actually want to obtain a smaller directed flow after the correction than it was before $\left|v_1^{\text{corr}}(y_{(0)} = 0)\right| < \left|v_1^{\text{raw}}(y_{(0)} = 0)\right|$. Different values of coefficient and also linear dependence were tested as a part of systematical uncertainty evaluation. Each track is finally weighted with the inverse of the efficiency $w_{\text{occup}} = 1/\varepsilon_{\text{occup}}$. The comparison of directed flow measurements before and after correction is presented on figure 5.5.

Chapter 6

Results on kaon flow

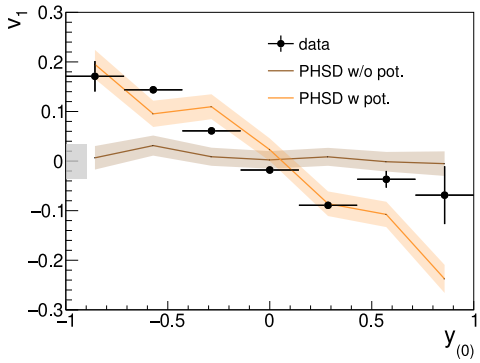

6.1 Application in differential kaon flow analysis

In this section, I will briefly summarize steps how the coefficients $v_n(\mathcal{C}, p_\mathrm{T}, y_{(0)})$ are obtained from the analysis of data collected from Au+Au collisions at $\sqrt{s_\mathrm{NN}} = 2.42\,\mathrm{GeV}$.

The first step is the data cleaning procedure followed by the event selection detailed in 3.2. For each selected event, the centrality $\mathcal{C}$ is determined using the comparison with Glauber model simulations [46]. Using the detected projectile fragments in the Forward Wall, the azimuthal angle of the event plane is estimated and its resolution is calculated as described above in sections 5.1.1 and 5.1.3.

All reconstructed particle tracks are examined and kaon candidates are selected via the methods depicted in chapter 4. Candidates are classified based on their transverse momentum p_T, normalized rapidity $y_{(0)}$, difference in azimuthal angle with respect to the event plane $\Delta\phi = \phi_\mathrm{K} - \Psi_1$, and the centrality of the event $\mathcal{C}$. For each group of kaon candidates, the background tracks are subtracted and the cleaned number of kaons is used for $\mathrm{d}N(\mathcal{C}, p_\mathrm{T}, y_{(0)})/\mathrm{d}\Delta\phi$ distribution, see figure 6.1. These spectra are then fitted with Fourier decomposition (5.4) with $m = 1$ and $k \leq 4$, and the obtained values v_{1-4}^obs are corrected for the event plane resolution (5.5). To get the final results for $v_n(\mathcal{C}, p_\mathrm{T}, y_{(0)})$ one must do the systematic uncertainty study.

6.2 Systematic uncertainty evaluation

To evaluate the systematic uncertainty of the flow coefficients $v_n(\mathcal{C}, p_\mathrm{T}, y_{(0)})$ I made several changes in the analysis procedure or varied the values of some parameters and observed how they affect the coefficients. Due to rather large statistical fluctuations, I averaged the differences $\delta v_n = \left|v_n - v_n^\mathrm{varied}\right|$ over all phase space bins ($N_\mathrm{PSB} = N_{p_\mathrm{T}}^\mathrm{bins} \cdot N_{y_{(0)}}^\mathrm{bins}$) in one centrality class

$$\sigma_\mathrm{sys}(\mathrm{variation}) = \frac{1}{N_\mathrm{PSB}} \sum_{i=1}^{N_\mathrm{PSB}} \frac{\left|v_n - v_n^\mathrm{varied}\right|}{\sqrt{\sigma_\mathrm{stat}^2(v_n) + \sigma_\mathrm{stat}^2(v_n^\mathrm{varied})}}. \tag{6.1}$$

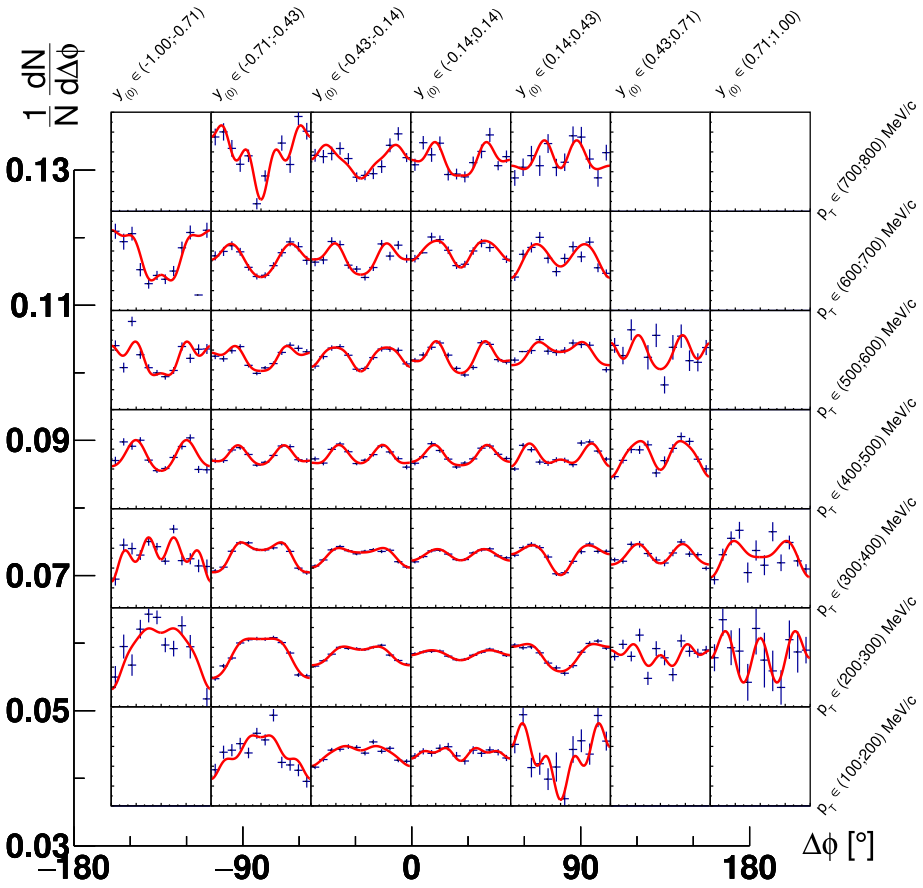

Figure 6.1: K^+ normalized azimuthal angle distributions w.r.t. event plane for centrality class $20-30\%$ and each phase space bin fitted with function (5.4) up to fourth order. For better readability, the enlarged axes are displayed on the side.

The total systematic error is then calculated as the square root of the sum of squares over all variations

$$\sigma_{\text{total sys}} = \sqrt{\sum_{\text{variations}} \sigma^2_{\text{sys}}(\text{variation})}. \tag{6.2}$$

The obtained values for K^+ are summarized in table 6.1.

6.3 Results of differential kaon flow analysis

The final results of the differential kaon flow analysis obtained via the procedures described in the previous sections and chapters would be presented only for K^+ and K^0_S. The negatively charged kaon production is too low for differential analysis, which is impeded because of background contamination. The obtained results for K^- and the integrated phase space will be mentioned at the end of this section.

The most compact representations of directed and elliptic flow analysis findings are the slope dependence of the directed flow $\left.\frac{\mathrm{d}v_1}{\mathrm{d}y_{(0)}}\right|_{y_{(0)}=0}$ plotted on figure 6.2, and rapidity integrated elliptic flow shown on figure 6.3 (both as a function of transverse momenta p_T for different centrality classes). The slope values of v_1 at midrapidity are obtained by fitting the individual directed flow spectra $v_1(y_{(0)})$ with a linear function in $y_{(0)}$ in the range $-0.4 < y_{(0)} < 0.4$. As the centrality of the collision decreases the magnitude of the slope increases. Except the agreement between K^+ and K^0_S one can observe that for low transverse momenta the slope is negative and with higher p_T it is rising and changes its sign always around $p_\mathrm{T} \approx 480\,\mathrm{MeV}/c$. The significant dependence observed for kaon flow on transverse momentum p_T was the original motivation for the differential analysis. From the flow symmetry requirement for the symmetrical collision system $v_1(y_{(0)} = 0) = 0$ and the observed rising trend of the directed flow slope, one can conclude that kaons (K^+ and K^0_S) exhibits positive directed flow for low p_T, the so-called antiflow. This opens the possibility of interpreting our results with the repulsive kaon-nucleon potential V_{KN}. The same outcome can be derived from the measured negative rapidity integrated elliptic flow, i.e. kaons are squeezed out of the collision zone. The absolute value of the potential is possible to deduce from the comparison with dedicated simulations using microscopic kinetic transport models. The parameter v_2 is slightly decreasing (or in absolute value increasing) with increasing transverse momenta. This behaviour is more pronounced with decreasing centrality, i.e. the slope of $v_2(p_\mathrm{T})$ is larger in semiperipheral collisions compared to most central collisions.

Unfortunately, the results on the differential flow of K^- were impossible to obtain. Although the absolute yield is not too distant from the yield of neutral kaons, the very low signal-to-background ratio makes this analysis futile. The remaining possibility was to integrate over the variables. Therefore, I select the centrality window $10 - 40\%$ (to omit the most central collisions where the event plane determination is problematic) and in the case of directed flow, the integration goes also over the transverse momentum and the elliptic flow is integrated over the rapidity, see figure 6.4. On that figure is also presented a comparison

collision centrality	v_1				v_2			
	$0-10\%$	$10-20\%$	$20-30\%$	$30-40\%$	$0-10\%$	$10-20\%$	$20-30\%$	$30-40\%$
flow methods	0.012	0.011	0.010	0.011	0.019	0.013	0.018	0.021
number of $\Delta\phi$ bins	0.003	0.003	0.003	0.003	0.008	0.006	0.005	0.007
number of harmonics	0.001	0.001	0.001	0.001	0.002	0.002	0.002	0.003
kaon identification	0.015	0.021	0.023	0.015	0.020	0.013	0.013	0.017
track quality cuts	0.011	0.010	0.011	0.012	0.019	0.009	0.009	0.013
occupancy corrections	0.013	0.008	0.004	0.003	0.006	0.005	0.003	0.003
background subtraction	0.017	0.021	0.021	0.020	0.012	0.007	0.006	0.009
total	0.031	0.035	0.035	0.030	0.037	0.023	0.025	0.032

Table 6.1: Summary table of the influence of individual variations on the directed and elliptic flow of K^+, respectively.

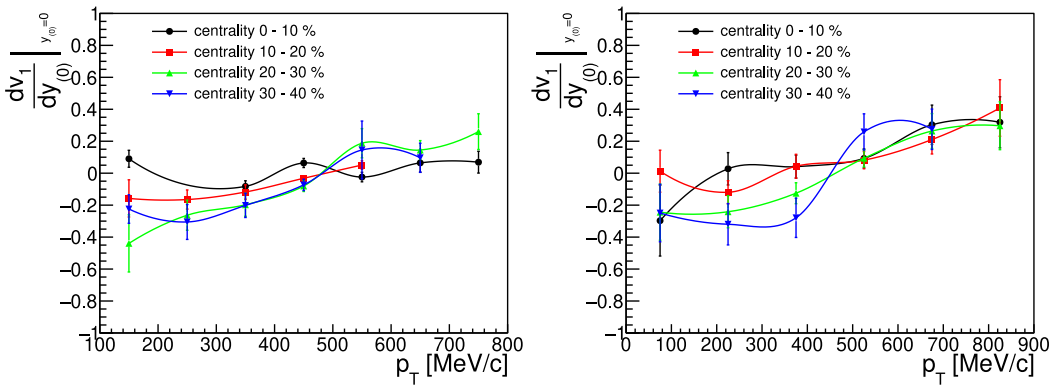

(a) K^+ (b) K^0_S

Figure 6.2: Dependence of the slope of the directed flow at midrapidity on the transverse momentum for different centrality classes.

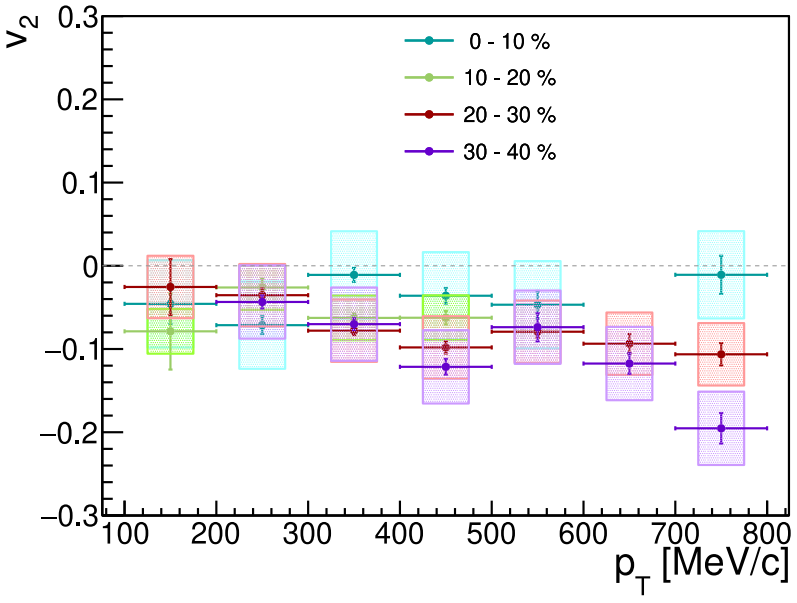

Figure 6.3: Comparison of rapidity integrated elliptic flow of K^+ for various collision centrality. The error bars displayed with lines indicate statistical uncertainties, and the boxes are for systematic uncertainties.

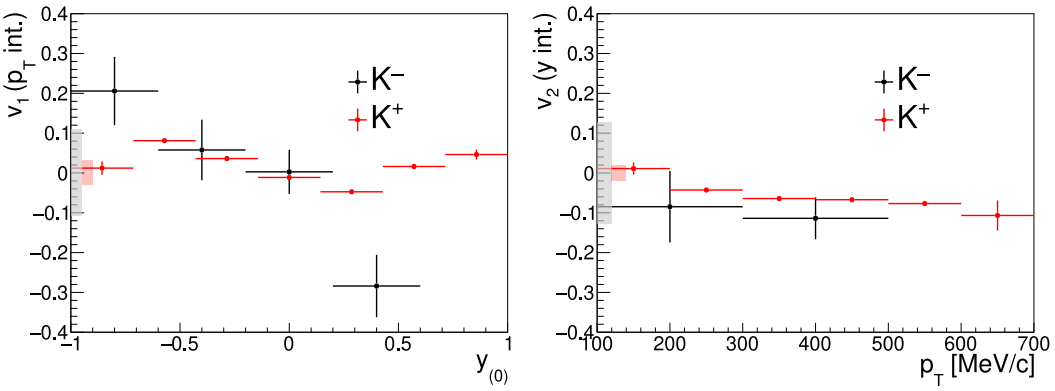

Figure 6.4: Measured p_{T}-integrated directed and rapidity integrated elliptic flow for K^- (black) and K^+ (red) in $10-40\%$ most central Au + Au collisions at $\sqrt{s_{\mathrm{NN}}} = 2.42\,\mathrm{GeV}$. Rectangles represent systematic uncertainty.

with the same integrated flow coefficients for K^+. However, it is difficult to make a strong statement on this comparison between charged kaons due to the size of uncertainties, the general trend is suggestive of being the same for both particle species. This finding is rather unexpected as the potentials V_{KN} and $V_{\bar{\mathrm{K}}\mathrm{N}}$ are predicted to be of opposite sign.

6.4 Comparison with models

In figure 6.5 the comparison of measured directed flow and the model predictions is presented. One can observe that most of the models predict, in agreement with HADES measurements, a rising trend of v_1 for high transverse momentum around mid-rapidity. On the other hand, only two models (GiBUU and PHSD) predict for low p_{T} the opposite, i.e., a decreasing trend which is observed in the experiment. Particularly good agreement in $v_1(y_{(0)})$ between data and model is achieved for PHSD with kaon-nucleon potential, which can be also seen in the comparison of slope of directed flow at midrapity displayed on figure 6.6. Pure cascade simulations, which do not contain this type of potential, are not able to reproduce the directed flow at low p_{T}. The addition of Skyrme potentials through the equation of state does not fundamentally change the outcome of the simulations. The UrQMD and SMASH models use high-mass nucleon resonances for the strangeness production, and kaon propagation is then governed only by the scattering of other particles [63]. These observations lead us to the conclusion that the incorporation of additional kaon-nucleon potentials into the model improves agreement with the directed flow measured by HADES.

The elliptic flow predictions are set side by side with the HADES measurement on figure 6.7. Similar findings to directed flow can be derived. The UrQMD model predicts zero v_2 independent of the simulation type. The SMASH cascade again agrees with UrQMD cascade, however, the inclusion of EoS squeezes the kaons slightly out of the dense environment resulting in a small negative elliptic flow especially at high transverse momentum. The GiBUU model with Skyrme type potentials follows well the trend of experimental data but significantly undershoots the elliptic flow at the quantitative level. On the other hand, when

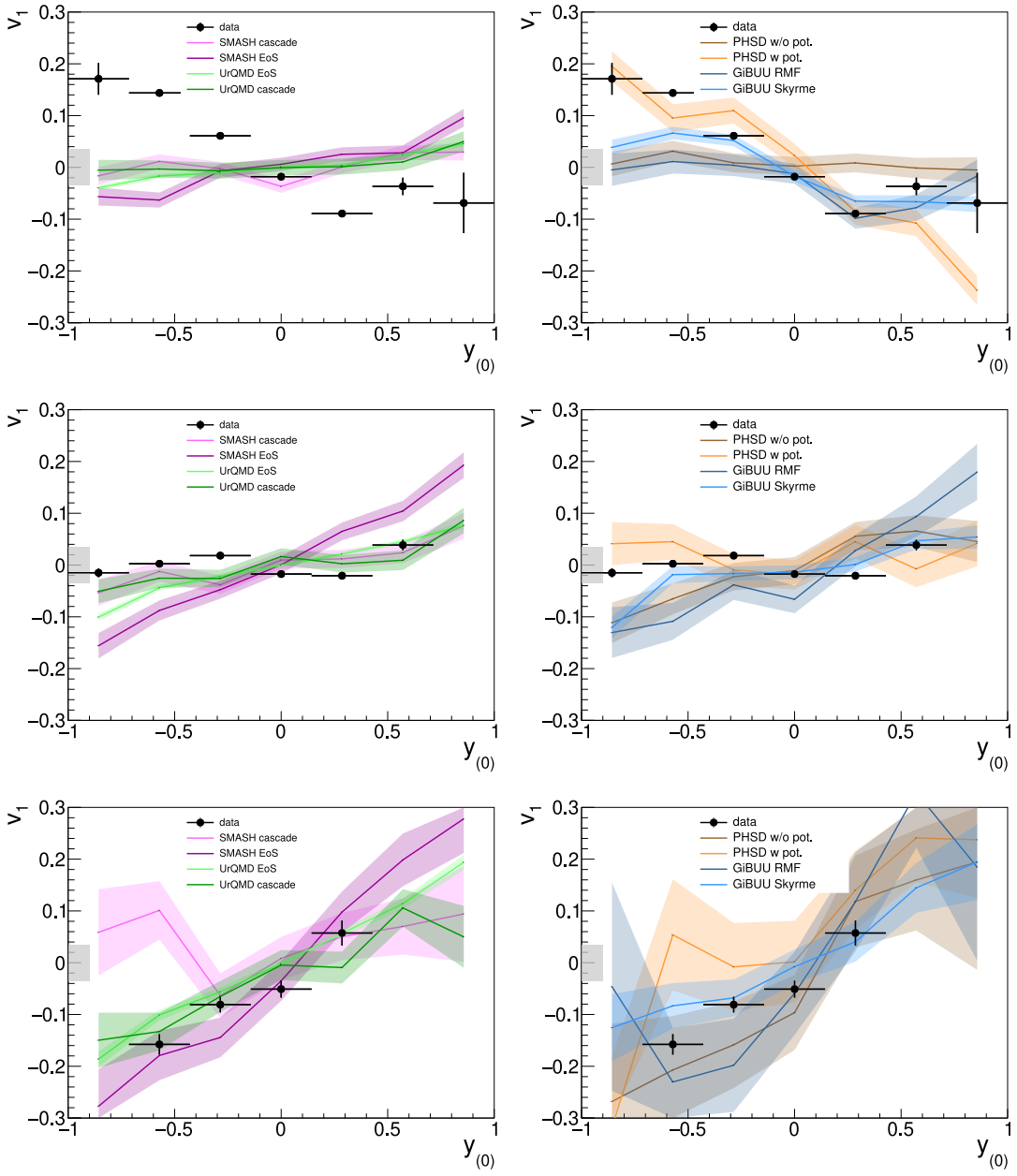

Figure 6.5: Close comparison of the results of the data analysis and the predictions of the directed flow for selected models. Upper row is for $p_{\mathrm{T}} \in (200, 300)\,\mathrm{MeV}/c$, middle row $p_{\mathrm{T}} \in (400, 500)\,\mathrm{MeV}/c$ and lower row $p_{\mathrm{T}} \in (700, 800)\,\mathrm{MeV}/c$. The gray box indicates the size of the systematic uncertainty of the data points.

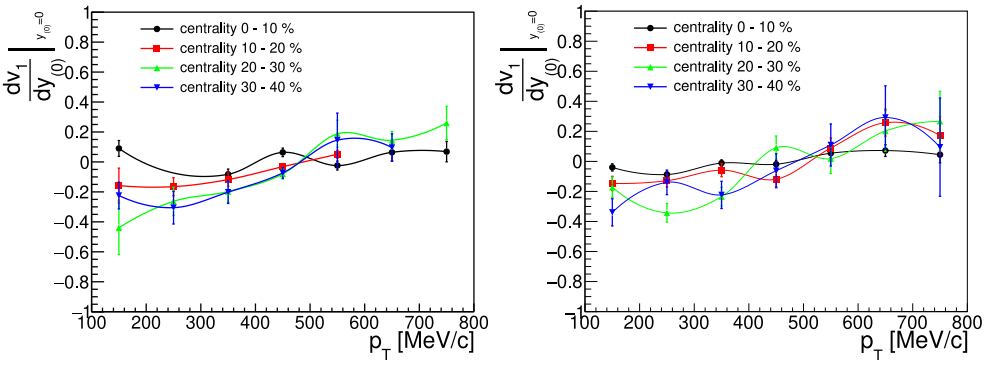

(a) experimental data (b) PHSD with KN pot.

Figure 6.6: The transverse momentum dependence of the slope of directed flow at midrapidity for different centrality classes. The experimental measurements on the left side and the prediction of the PHSD model on the right.

the RMF mode of simulation is used (which also includes the KN potential), the best agreement with the experimental data is achieved. In the case of the PHSD model, the inclusion of the KN potential does not play as an important role as it did in the directed flow. The qualitative agreement between the data and the PHSD is very good, but the experimental data suggest a slightly stronger kaon squeeze-out. The centrality dependence of the rapidity integrated elliptic flow is the subject of the figure 6.8 where the GiBUU RMF model was selected as it was found to best describe the experimental data.

The analysis of the flow of antikaons, as was mentioned earlier, was much more complicated for experimental data, and thus the integration over centrality and transverse momentum for v_1, respective rapidity for v_2 was unavoidable. The model prediction with the same assumptions is shown on figure 6.9. Although the statistical and systematic uncertainties of the experimental data points are significant, one can make an interesting observation: contrary to the case of K^+ directed flow where SMASH and UrQMD curves were quite distant from the HADES measurement (see figure 6.10), the antikaons are well described by these models even in the cascade mode where no potentials are included. The same holds true for PHSD models where the option without the KN potential is in better agreement with the data points than the PHSD with the KN potential. The elliptic flow is very close to zero in almost all transport models, where the data points suggest a small squeeze-out of antikaons (negative v_2). The case of negative kaons is very intricate not only due to limited statistics and thus large uncertainty, but also due to the fact that a considerable fraction ($\approx \frac{1}{2}$) of K^- originates from ϕ meson decay [64].

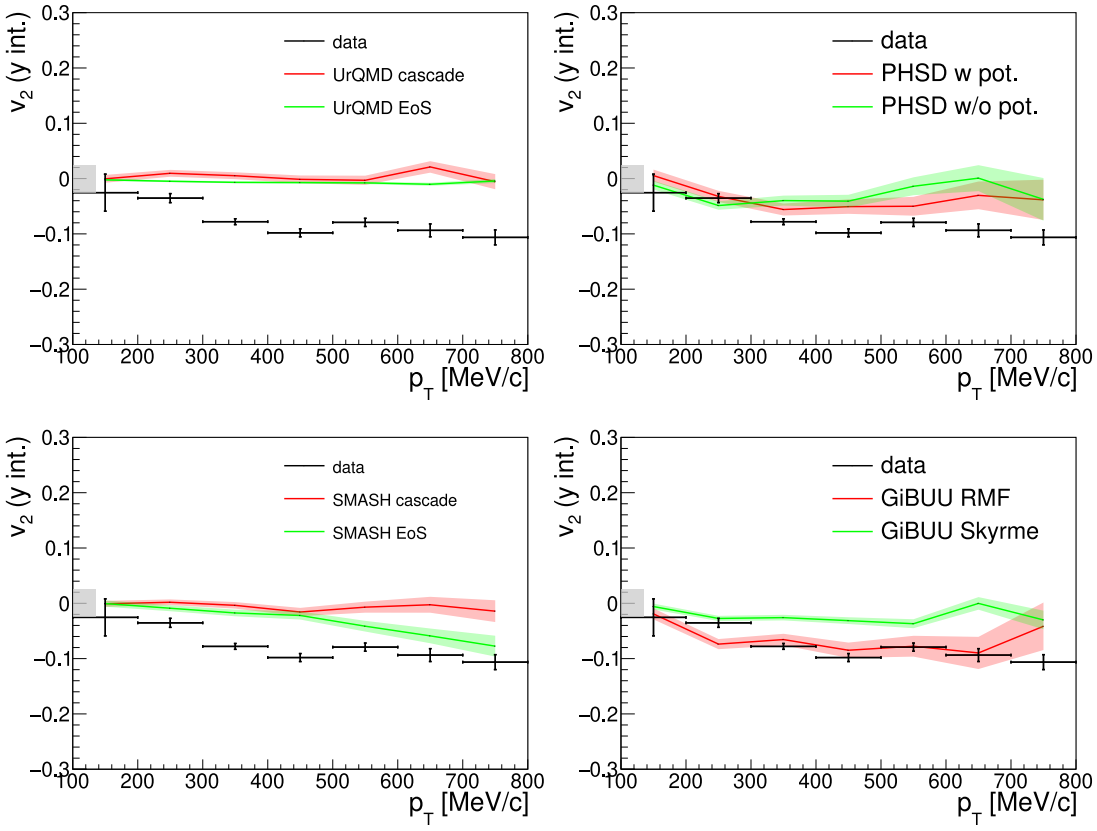

Figure 6.7: Elliptic flow of positively charged kaons measured in $20-30\%$ most central Au + Au collisions at beam energy $1.23A$ GeV confronted with selected transport model simulations. The gray box indicates the size of the systematic uncertainty of the data points.

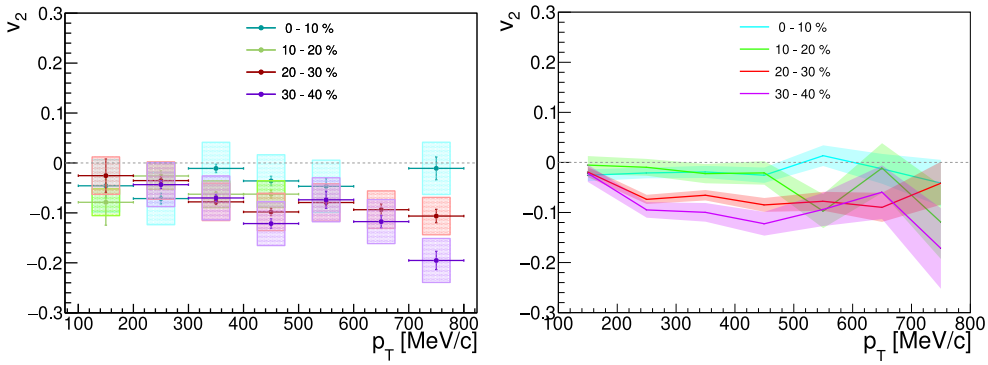

(a) experimental data (b) GiBUU RMF

Figure 6.8: The transverse momentum dependence of the rapidity integrated elliptic flow for different centrality classes. The experimental measurements on the left side and the prediction of the GiBUU model on the right.

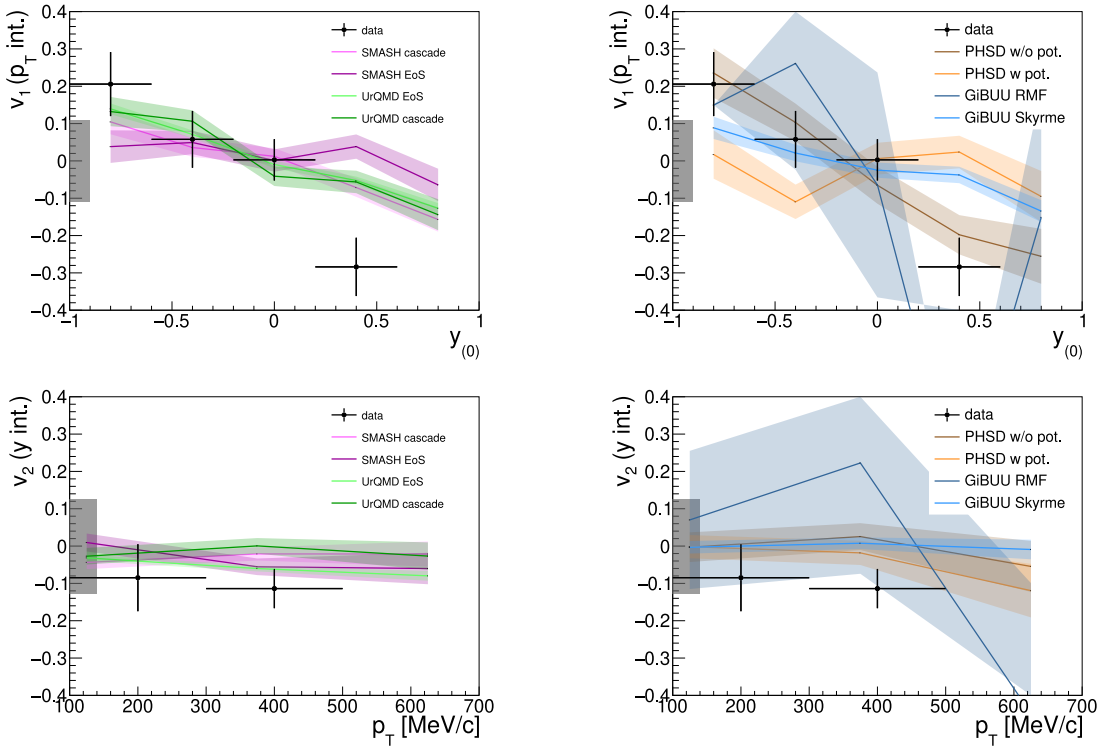

Figure 6.9: Measurements of directed and elliptic flow for K^- are set side by side to simulations obtained from selected models. The gray box indicates the size of the systematic uncertainty of the data points.

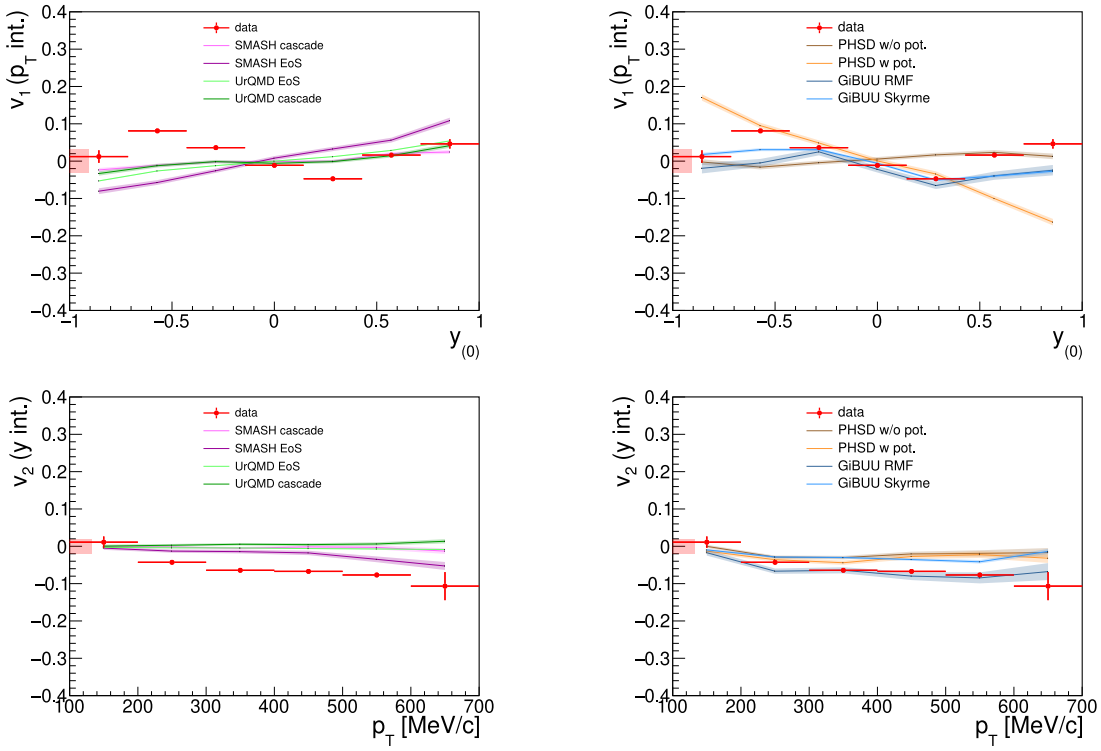

Figure 6.10: K^+ measured and model predicted directed and elliptic flow within the range of integration of flow measurement for K^-. The red box indicates the size of the systematic uncertainty of the data points.

Conclusion

In this thesis, I focused on the analysis of kaon flow in Au + Au collisions at kinetic beam energy 1.23A GeV measured with the HADES spectrometer during April and May 2012.

The study of strangeness around the NN threshold energy is one of the pillars of the HADES collaboration physics program, since the strange hadrons are considered a good probe of the processes taking place inside the hot and dense nuclear matter. Thanks to the nowadays solitary investigation of heavy-ion collisions at $\sqrt{s_{\mathrm{NN}}} \approx 2.5\,\mathrm{GeV}$ (apart from experiments with SIS18 at GSI, there were pioneering experiments at Bevalac/LBL in the 1980s and 1990s), it gives HADES a unique opportunity to study very rare probes for the first time or at least significantly improve the existing results. The spectrometer is continuously upgraded to provide further insight on the interesting state of strongly interacting matter, which can also be observed not only in our laboratory but in the Universe as well, e.g., in the neutron star merge.

During the mentioned gold beam time, HADES has recorded over 7 billion events from which 2.2 billions were selected for physics analysis. This remarkable data set allowed one to study very sensitive observables such as differential transverse flow even for subthreshold-produced kaons. After careful cleaning of the recorded events and sorting of the identified tracks, the kaons were identified. The charged kaon candidates were chosen on the basis of the track quality parameters and specific energy losses in the MDC and TOF detectors. The neutral kaon candidates were reconstructed using their decay products (the charged pion channel is the most convenient from an experimental point of view), and for the pion pair selection, machine learning algorithms were trained and applied. The background tracks were subtracted with the fitting procedure and the mixed event technique for charged and neutral kaons, respectively. The azimuthal angle distributions of kaons with respect to the first harmonic of the reaction plane were later fitted with Fourier decomposition and the obtained coefficients v_n^{obs} were corrected for the event plane resolution. Systematic uncertainties were determined from the variation of several values of the analysis parameters.

From the results on the directed and elliptic flow of (anti)kaons, I made the following observations:

- directed flow of K^+ is strongly dependent on transverse momentum,
- both $|v_1|$ and $|v_2|$ of K^+ is decreasing with increasing collision centrality,
- elliptic flow of K^+ is approximately constant as a function of rapidity and decreases towards higher transverse momentum,
- there is no significant difference in flow of K^+ and $\mathrm{K}^0_{\mathrm{S}}$,
- directed flow of K^- integrated over transverse momentum exhibits antiflow pattern,
- elliptic flow of K^- is not significantly different from zero (probably is slightly negative).

Although it is not appropriate to compare these results directly with other measurements done by KaoS, FOPI, and STAR collaborations (due to slightly different kinetic beam energy and/or due to different collision system sizes), they can be viewed as useful guidelines. The results of kaon flow presented in this thesis are in good qualitative agreement with the published data reviewed in section 1.3.1. In particular, there is agreement with all experiments that the elliptic flow of K^+ is negative and approximately constant function of rapidity. One can also see a correspondence with FOPI that the directed flow of K^+ is positive for low transverse momentum and drops to negative values for $\frac{p_T}{m} > 1$, available results from STAR are for higher p_T where a similarity can be found in the rising trend of $v_1(y)$ of kaons. The identical observed flow patterns of K^+ and K^0_S are confirmed with the STAR measurements, together with qualitatively very similar tendencies of K^- flow. The decreasing trend of the absolute value of transverse flow for more central collisions was also found by the FOPI collaboration, as well as the observation of antiflow for K^-.

Additionally, I made a comparison with the selected kinetic transport models: SMASH, UrQMD, PHSD, and GiBUU. For the positively charged kaons, the best agreement with the presented experimental data belongs to PHSD with the KN potential switched on. On the opposite side are models which do not use any potentials (the simulations were performed in the so-called cascade mode). A surprise was to find that for K^- these models (where no potentials were used) predict the closest values to the HADES measurements. More detailed understanding of why some models work better for K^+ and not so well for K^- and vice versa is desirable.

Finally, the HADES collaboration recorded during March 2019 about two times more collisions of Ag + Ag at $\sqrt{s_{NN}} = 2.55\,\text{GeV}$ which exactly corresponds to K^+ production threshold energy. The analysis of these data might be thus very interesting and can provide even more precise and differential results on kaon flow in heavy-ion collisions.

Bibliography

[1] J. Rafelski. Melting hadrons, boiling quarks. *European Physical Journal A* **51** (9): 114. 2015.

[2] B. P. Abbott *et al.* (LIGO Scientific Collaboration and Virgo Collaboration). GW170817: Observation of Gravitational Waves from a Binary Neutron Star Inspiral. *Physical Review Letters* **119** : 161101. 2017.

[3] T. Galatyuk, P. M. Hohler, R. Rapp, F. Seck, and J. Stroth. Thermal dileptons from coarse-grained transport as fireball probes at SIS energies. *European Physical Journal A* **52** (5). 2016.

[4] M. L. Miller, K. Reygers, S. J. Sanders, and P. Steinberg. Glauber Modeling in High-Energy Nuclear Collisions. *Annual Review of Nuclear and Particle Science* **57** (1): 205-243. 2007.

[5] S. Mandelstam. Determination of the Pion-Nucleon Scattering Amplitude from Dispersion Relations and Unitarity. General Theory. *Physical Review* **112** : 1344–1360. 1958.

[6] M. Tanabashi *et al.* (Particle Data Group). Review of Particle Physics. *Physical Review D* **98** : 030001. 2018.

[7] H. Oeschler. Strangeness production at 1-2 A GeV. *Progress in Particle and Nuclear Physics* **62** (2): 433–438. 2009.

[8] C. M. Ko. Effect of final state interactions on subthreshold K^- production in heavy-ion collisions. *Physics Letters B* **138** (5-6): 361–364. 1984.

[9] D. B. Kaplan and A. E. Nelson. Strange goings on in dense nucleonic matter. *Physics Letters B* **175** (1): 57–63. 1986.

[10] G. Brown, K. Kubodera, and M. Rho. Strangeness condensation and "clearing" of the vacuum. *Physics Letters B* **192** (3-4): 273–278. 1987.

[11] C. H. Lee, G. E. Brown, and M. Rho. Kaon condensation in "nuclear star" matter. *Physics Letters B* **335** (3-4): 266–272. 1994.

[12] T. Muto and T. Tatsumi. Theoretical aspects of kaon condensation in neutron matter. *Physics Letters B* **283** (3-4): 165–170. 1992.

[13] M. Lutz, A. Steiner, and W. Weise. Kaons in baryonic matter. *Nuclear Physics A* **574** (4): 755–787. 1994.

[14] H. Yabu, S. Nakamura, F. Myhrer, and K. Kubodera. Effective kaon mass in baryonic matter and kaon condensation. *Physics Letters B* **315** (1-2): 17–23. 1993.

[15] P. Braun-Munzinger, K. Redlich, and J. Stachel. *Particle production in heavy ion collisions* (World Scientific, 2004), pp. 491–599. `https://www.worldscientific.com/doi/pdf/10.1142/9789812795533_0008`.

[16] B. Borasoy. Introduction to chiral perturbation theory. *Springer proceedings in physics* **118** : 1–26. 2008.

[17] A. E. Nelson and D. B. Kaplan. Strange condensate realignment in relativistic heavy ion collisions. *Physics Letters B* **192** (1): 193 - 197. 1987.

[18] G. Brown, K. Kubodera, M. Rho, and V. Thorsson. A novel mechanism for kaon condensation in neutron star matter. *Physics Letters B* **291** (4): 355 - 362. 1992.

[19] G. Brown, C.-H. Lee, M. Rho, and V. Thorsson. From kaon-nuclear interactions to kaon condensation. *Nuclear Physics A* **567** (4): 937 - 956. 1994.

[20] N. Kaiser, P. Siegel, and W. Weise. Chiral dynamics and the low-energy kaon-nucleon interaction. *Nuclear Physics A* **594** (3): 325 - 345. 1995.

[21] M. Lutz. Nuclear kaon dynamics. *Physics Letters B* **426** (1): 12 - 20. 1998.

[22] G. Mao *et al.*. Kaon effective mass and energy from a novel chiral SU(3)-symmetric Lagrangian. *Physical Review C* **59** : 3381–3385. 1999.

[23] G. Q. Li and C. M. Ko. Kaon flow in heavy-ion collisions. *Nuclear Physics A* **594** (4): 460–482. 1995.

[24] S. Weinberg. Pion Scattering Lengths. *Physical Review Letters* **17** : 616–621. 1966.

[25] Y. Tomozawa. Axial-vector coupling constant renormalization and the meson-baryon scattering lenghts. *Il Nuovo Cimento A* **46** (4): 707–717. 1966.

[26] P. B. Demorest, T. Pennucci, S. M. Ransom, M. S. E. Roberts, and J. W. T. Hessels. A two-solar-mass neutron star measured using Shapiro delay. *Nature* **467** (7319): 1081–1083. 2010.

[27] G. Q. Li, C. M. Ko, and B. A. Li. Kaon flow as a probe of the kaon potential in nuclear medium. *Physical Review Letters* **74** (2): 235–238. 1995.

[28] G. Li, C. Ko, and G. Brown. Kaon azimuthal distributions in heavy-ion collisions. *Physics Letters B* **381** (1): 17 - 22. 1996.

[29] Z. S. Wang, C. Fuchs, A. Faessler, and T. Gross-Boelting. Kaon squeeze-out in heavy ion reactions. *European Physical Journal A* **5** : 275–283. 1999.

[30] C. A. Ogilvie (E802 and E917 Collaboration). Kaon production in Au + Au collisions at the AGS. *Nuclear Physics A* **630** : 571C–581C. 1998.

[31] S. Voloshin (E877 Collaboration). Anisotropic flow of identified particles in Au + Au collisions at AGS energy. *Nuclear Physics A* **638** : 455C–458C. 1998.

[32] J. L. Ritman *et al.* (FOPI collaboration). On the transverse momentum distribution of strange hadrons produced in relativistic heavy ion collisions. *Zeitschrift für Physik A Hadrons and Nuclei* **352** (4): 355–357. 1995.

[33] B.-A. Li and A. T. Sustich. Differential Flow in Heavy-Ion Collisions at Balance Energies. *Physical Review Letters* **82** (25): 5004–5007. 1999.

[34] B. A. Li, B. Zhang, A. T. Sustich, and C. M. Ko. Kaon differential flow in relativistic heavy-ion collisions. *Physical Review C* **60** (3): 4. 1999.

[35] M. S. Abdallah *et al.* (STAR Collaboration). Flow and interferometry results from Au+Au collisions at $\sqrt{s_{NN}} = 4.5$ GeV. *Physical Review C* **103** : 034908. 2021.

[36] A. Förster *et al.* (KaoS collaboration). Review of the results of the KaoS Collaboration. *Journal of Physics G* **31** (6): S693–S700. 2005.

[37] M. S. Abdallah *et al.*. Disappearance of partonic collectivity in $\sqrt{s_{NN}} = 3$ GeV Au+Au collisions at RHIC. `arXiv:2108.00908v1`.

[38] V. Zinyuk *et al.* (FOPI collaboration). Azimuthal emission patterns of K^+ and of K^- mesons in Ni + Ni collisions near the strangeness production threshold. *Physical Review C* **90** (2): 025210. 2014.

[39] G. Roche *et al.* (DLS collaboration). First Observation of Dielectron Production in Proton-Nucleus Collisions below 10 GeV. *Physical Review Letters* **61** (9): 1069–1072. 1988.

[40] P. Kienle. The SIS/ESR-project at GSI: Present and future. in *The Nuclear equation of state. Pt. A: Discovery of nuclear shock waves and the EOS. Proceedings, NATO Advanced Study Institute, Peniscola, Spain, May 22 - June 3, 1989*, edited by W. Greiner and H. Stoecker. pp. 463–476. Springer, Boston, MA. 1989.

[41] A. Yegneswaran *et al.* (DLS collaboration). The dilepton spectrometer. *Nuclear Inst. and Methods in Physics Research, A* **290** (1): 61–75. 1990.

[42] HADES collaboration. Internal Materials.

[43] G. Agakichiev *et al.* (HADES collaboration). The high-acceptance dielectron spectrometer HADES. *European Physical Journal A* **41** (2): 243–277. 2009.

[44] L. Fabbietti. *Study of the* e^+e^- *pair acceptance in the dilepton spectrometer HADES*. PhD thesis. Technische Universität München, Physics Department. 2003.

[45] R. J. Glauber. Cross Sections in Deuterium at High Energies. *Physical Review* **100** : 242–248. 1955.

[46] J. Adamczewski-Musch *et al.* (HADES collaboration). Centrality determination of Au + Au collisions at 1.23A GeV with HADES. *European Physical Journal A* **54** (5): 85. 2018.

[47] T. Scheib. Λ *and* K^0_s *Production in Au+Au Collisions at* 1.23 *A*GeV. PhD thesis. Johann Wolfgang Goethe-Universität in Frankfurt am Main, Physics Department. 2017.

[48] P. Sellheim. *Reconstruction of the low-mass dielectron signal in* 1.23 *A*GeV *Au+Au collisions*. PhD thesis. Johann Wolfgang Goethe-Universität in Frankfurt am Main, Physics Department. 2017.

[49] J. Adamczewski-Musch *et al.* (HADES collaboration). Charged pion production in $\mathbf{Au + Au}$ collisions at $\sqrt{\mathbf{s_{NN}}} = 2.4\mathbf{GeV}$. *to be published in EPJA* . 2020.

[50] M. Lorenz. *Vector meson production in* p + Nb *reactions and statistical particle production in* Ar + KCl *collisions*. PhD thesis. Johann Wolfgang Goethe-Universität in Frankfurt am Main, Physics Department. 2012.

[51] A. Hoecker *et al.*. TMVA: Toolkit for Multivariate Data Analysis. *Proceedings of Science* **050** : 040. 2007.

[52] A. M. Poskanzer and S. A. Voloshin. Methods for analyzing anisotropic flow in relativistic nuclear collisions. *Physical Review C* **58** (3): 1671–1678. 1998.

[53] B. Kardan. Flow harmonics of Au+Au collisions at 1.23 AGeV with HADES. *Journal of Physics: Conference Series* **742** (1). 2016.

[54] J. Adamczewski-Musch *et al.* (HADES Collaboration). Directed, elliptic and higher order flow harmonics of protons, deuterons and tritons in Au+Au collisions at $\sqrt{s_{\mathrm{NN}}} = 2.4\,GeV$. *Physical Review Letters* **125** : 262301. 2020.

[55] S. Voloshin and Y. Zhang. Flow study in relativistic nuclear collisions by Fourier expansion of azimuthal particle distributions. *Zeitschrift fur Physik C* **70** (4): 665–671. 1996.

[56] P. Danielewicz and G. Odyniec. Transverse momentum analysis of collective motion in relativistic nuclear collisions. *Physics Letters B* **157** (2-3): 146–150. 1985.

[57] J.-Y. Ollitrault. Reconstructing azimuthal distributions in nucleus-nucleus collisions. `arXiv:nucl-ex/9711003`.

[58] W. Reisdorf *et al.* (FOPI collaboration). Systematics of pion emission in heavy ion collisions in the 1A GeV regime. *Nuclear Physics A* **781** (3): 459-508. 2007.

[59] B. B. Back *et al.* (PHOBOS collaboration). Pseudorapidity and Centrality Dependence of the Collective Flow of Charged Particles in Au+Au Collisions at $\sqrt{s_{NN}} = 130$ GeV. *Physical Review Letters* **89** : 222301. 2002.

[60] A. Prozorov. Simulation study of effects induced by final granularity of detector in particle flow. *Journal of Physics: Conference Series* **1667** : 012034. 2020.

[61] M. Grunwald. Flow correction for 1.23*A* GeV Au+Au collisions at the HADES experiment. in *Photonics Applications in Astronomy, Communications, Industry, and High Energy Physics Experiments 2020*, edited by R. S. Romaniuk and M. Linczuk. p. 26. SPIE. 2020.

[62] F. J. Kornas. Λ polarization in Au+Au collisions at $\sqrt{s_{\mathrm{NN}}} = 2.4\,\mathrm{GeV}$ measured with HADES. in *The XVIII International Conference on Strangeness in Quark Matter (SQM 2019)*, edited by D. Elia, G. E. Bruno, P. Colangelo, and L. Cosmai. pp. 435–439. Cham. 2020. Springer International Publishing.

[63] V. Steinberg *et al.*. Strangeness production via resonances in heavy-ion collisions at energies available at the GSI Schwerionensynchrotron. *Physical Review C* **99** (6): 064908. 2019.

[64] J. Adamczewski-Musch *et al.* (HADES collaboration). Deep sub-threshold ϕ production in Au+Au collisions. *Physics Letters B* **778** : 403–407. 2018.